Economic Geology, v. 112, pp. 799–827

Geology and Genesis of the Cerro la Mina Porphyry-High Sulfidation Au (Cu-Mo) Prospect, Mexico

Nicholas H. Jansen,[1,†] J. Bruce Gemmell,[1] Zhaoshan Chang,[1,*] David R. Cooke,[1] Fred Jourdan,[2] Robert A. Creaser,[3] and Pete Hollings[4]

[1] *CODES, ARC Centre for Excellence in Ore Deposits, University of Tasmania, Private Bag 126, Hobart, Tasmania 7001, Australia*

[2] *Department of Applied Geology and John de Laeter Centre for Geochronology, Curtin University, GPO Box U1987, Perth, Western Australia 6845, Australia*

[3] *Department of Earth and Atmospheric Sciences, University of Alberta, 1-26 Earth Sciences Building, Edmonton, Alberta T6G 2E3, Canada*

[4] *Geology Department, Lakehead University, 955 Oliver Road, Thunder Bay, Ontario P7B 5E1, Canada*

Abstract

The Cerro la Mina Au (Cu-Mo) porphyry-high sulfidation prospect is located in Chiapas State, southeastern Mexico, outside of the major metallogenic provinces of Mexico. The prospect is hosted by Pleistocene alkaline volcanic rocks of the Chiapanecan volcanic arc that formed in a complex triple-junction tectonic setting. Cerro la Mina's stratigraphy comprises pyroclastic flows that were intruded by monzodiorites and diorites at 1.04 ± 0.04 Ma (U-Pb, zircon), and that were overlain by debris flows and synvolcanic trachyandesite domes. The volcanic stratigraphy of Cerro la Mina is dominated by pyroclastic flows and rare basalts that are cut by the Cerro la Mina breccia pipe, a matrix-rich granular, vertically oriented, downward-tapering, polymict lithic rock unit that is host to all of the significant alteration and mineralization. A NW-trending sinistral wrench fault, which was active throughout the history of Cerro la Mina, is responsible for dismembering the prospect after mineralization.

The magmatic hydrothermal system was composed of early porphyry-style potassic veins (quartz + K-feldspar ± biotite) and stage 1 pyrite that are preserved in clasts within the breccia pipe, suggesting that brecciation disrupted an embryonic porphyry system. Late potassic alteration occurred after the formation of the breccia pipe, as its matrix is strongly K-feldspar altered. Hydrothermal fluids then produced phyllic alteration composed of quartz, muscovite, illite, illite-smectite, and chlorite that is associated with stage 2 pyrite ± chalcopyrite ± molybdenite ± quartz veins. An unusual zoned pattern of advanced argillic-argillic alteration overprinted potassic and phyllic alteration. This zoning included a low-temperature (<110°C) halloysite + kaolinite that extends from 800 to 250 m below present-day surface and is deeper than higher temperature (>120°C) quartz + dickite ± kaolinite ± pyrophyllite ± alunite that occurs from 250 m to the present-day surface. The advanced argillic-argillic altered rocks host the most significant Au-Cu mineralization, which is associated with stage 3 marcasite, sphalerite, galena, and barite, and stage 4 arsenian pyrite ± enargite ± covellite.

The magmatic hydrothermal system at Cerro la Mina began sometime between monzodiorite emplacement (1.04 ± 0.04 Ma; zircon U-Pb) and the precipitation of porphyry stage 2 molybdenite at 780 ± 10 ka (Re-Os). $^{40}Ar/^{39}Ar$ dating of biotite (689 ± 13 ka) records the age at which the hydrothermal system cooled below the biotite closure temperature of ~300°C and provides a maximum estimate for the onset of advanced argillic-argillic alteration. Sulfur isotope results of sulfides (–2.5 to +4.9‰; mean +0.7‰; n = 20) and a sulfate (barite; +10.5‰; n = 1) suggest a magmatic source of sulfur for all four stages of mineralization. The lack of residual quartz, rare alunite, and anomalous halloysite-kaolinite alteration may be explained by the high acid-buffering capacity of alkaline volcanic host rocks, high CO_2 contents of the alkaline magma, and/or potentially by a highly reduced magmatic hydrothermal fluid.

At the regional metallogenic scale, the Cerro la Mina prospect along with the nearby Santa Fé mine and Campamento deposit represent parts of a porphyry copper system—specifically, a porphyry/high-sulfidation, proximal skarn and intermediate sulfidation deposit, respectively. The characteristics of Cerro la Mina (i.e., anomalous halloysite-kaolinite alteration) broaden the window for additional discoveries to be made in the porphyry-epithermal environment.

Introduction

The Cerro la Mina porphyry-high sulfidation Au (Cu-Mo) epithermal prospect is part of Fortune Bay's (formerly Linear Resources, Linear Gold, and Brigus Gold) Ixhuatán concession in Chiapas State, southeastern Mexico (Fig. 1). In 2006, exploration drilling intersected a near-surface, supergene oxidized gold zone overlying Au (Cu-Mo) and sulfide mineralization. From a total of 64 drill holes, approximately 22,000 m were drilled at Cerro la Mina before exploration ceased in 2009. No resource estimate was published for the Cerro la Mina prospect.

Porphyry and epithermal occurrences in the state of Chiapas are located outside the major metallogenic provinces of Mexico and are hosted in significantly younger volcanic rocks (<5 Ma; Damon and Motesinos, 1978; Camprubí and Albinson, 2007; Valencia-Moreno et al., 2007). Thus far, the Santa

† Corresponding author: e-mail, njansenmail@gmail.com
* Present address: James Cook University, 1 James Cook Dr, Townsville City, Queensland 4811, Australia.

Submitted: May 8, 2014
Accepted: November 30, 2016

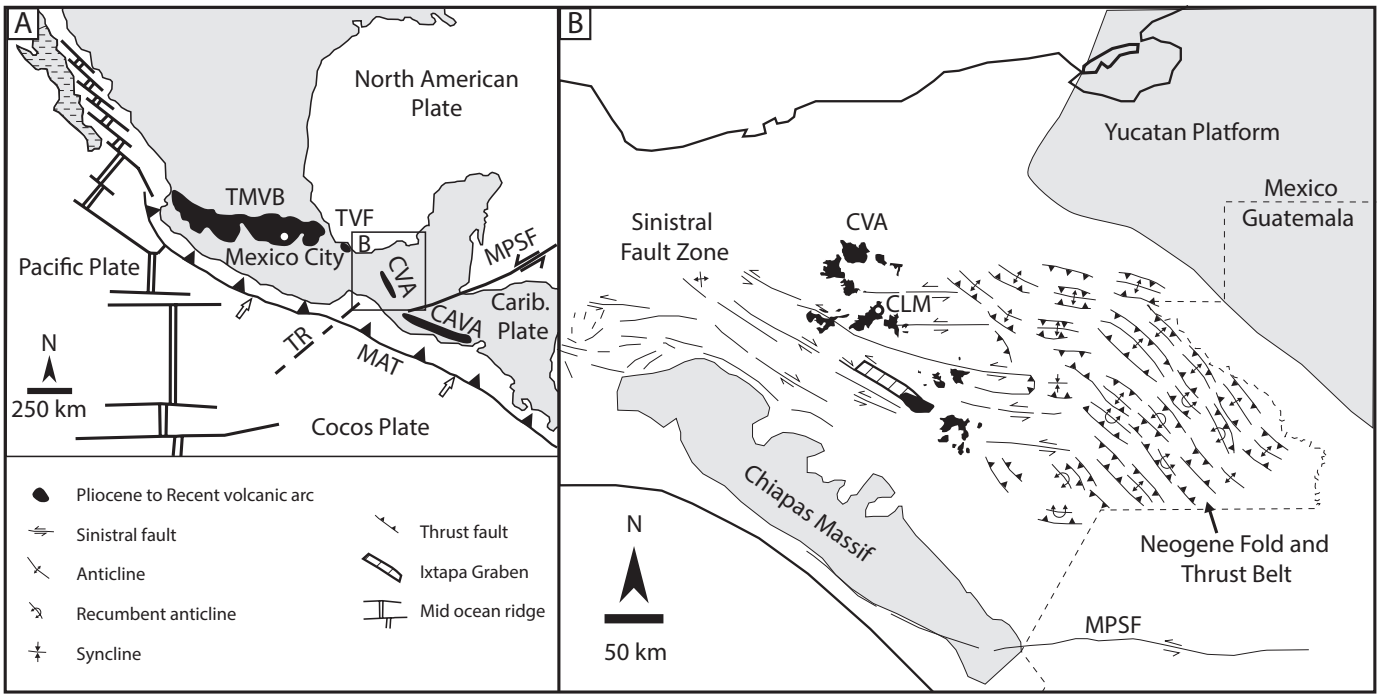

Fig. 1. Volcanic rocks and structure of southeastern Mexico. A. Tectonic map and distribution of volcanic arcs of Mexico and Central America from Cenozoic to Recent. Modified from Robin (1982), García-Palomo et al. (2004) and Mora et al. (2007). B. Generalized structural map of southeastern Mexico and location of Chiapanecan volcanic arc volcanism. Modified from García-Palomo et al., 2004. Abbreviations: CAVA = Central American volcanic field, CLM = Cerro la Mina prospect, CVA = Chiapanecan volcanic arc, MAT = Middle American Trench, MPSF = Motagua-Polochic sinistral fault, TMVB = Trans Mexican volcanic belt, TR = Tehuantepec Ridge, TVF = Tuxtlas volcanic field.

Fé Cu-Au skarn deposit, Campamento Au-Ag epithermal deposit, Cerro la Mina Au (Cu-Mo) prospect, and Tolimán Cu porphyry are the only areas for which Cu-Mo-Ag-Au occurrences have been reported in Chiapas (Sillitoe, 1976; Damon et al., 1983; Pantoja, 1991; Barton et al., 1995; Jansen, 2007; Miranda-Gasca et al., 2009; Jansen, 2012). This paper documents the geologic features of the Cerro la Mina prospect in order to provide further insight into a poorly understood metallogenic region of Mexico. This project was pursued by drill hole logging and petrography to describe the geology, alteration and mineralization, geochronological dating, and a sulfur isotope study to determine the source of fluids. A discussion comparing the Cerro la Mina prospect with the nearby (20-km) El Chichón volcano, which has erupted lithic fragments of porphyry-style mineralization (Luhr, 1983; Rye et al., 1984; Luhr and Logan, 2002; Rye, 2005), may provide some suggestions as to the genesis of the porphyry-epithermal prospect. The understanding of the Cerro la Mina prospect opens new frontiers for discoveries in an underexplored region with a complex tectonic setting and uncommon styles of alteration and mineralization.

Tectonic Setting and Regional Geology

Tectonic setting

Cerro la Mina is located in the complex triple junction area of southeastern Mexico. A series of left-lateral strike-slip faults, known as the Motagua-Polochic sinistral fault, were produced by the eastward migration of the Caribbean plate relative to the North American plate and this sinistral fault now separates the North American and Caribbean plates (Fig. 1A). A zone of convergence occurs with the subduction of the oceanic Cocos plate under both the continental North American plate and the mostly oceanic Caribbean plate along the Middle American trench (Nixon, 1982; Burbach et al., 1984). The subducting Cocos plate contains the Tehuantepec ridge, which is being subducted toward the northeast (Fig. 1A); its onshore projection lies below the Cerro la Mina prospect.

The triple-junction setting resulted in two structural zones in southeastern Mexico, namely a Neogene fold-and-thrust belt and the strike-slip fault zone (Fig. 1B; Guzman-Speziale and Meneses-Rocha, 2000). The two zones are bounded to the south by the Chiapas massif and to the north by the Yucatan platform (Fig. 1B). The fold-and-thrust belt has an elongated structural trend, convex to the northeast, defined by long, narrow anticlines offset along their flanks by reverse faults that have generally overthrust the intervening synclines (Fig. 1B; Mandujano-Velazquez and Keppie, 2009). The strike-slip fault zone is ~130 km wide and ~360 km long, composed of a set of upthrown and downthrown blocks, bounded by left-lateral strike-slip faults and is interpreted to be an extension of the Motagua-Polohic fault (Fig. 1B; Meneses-Rocha, 2001).

Regional geology

The geology of Chiapas State is summarized in Table 1 and consists of a pre-Mesozoic metamorphic, igneous, and sedimentary basement overlain or intruded by Mesozoic sedimentary rocks and Cenozoic volcanic and igneous rocks (Fig.

Table 1. Stratigraphic Summary of Chiapas State Geology

Formation	Thickness (m)	Eon, period, or epoch	Description
n.a.		Holocene	Silt, sand, and clay deposits
El Chichón and Tacaná		Holocene	Trachyandesite pyroclastic rocks (El Chichon), lahar and andesitic volcanic breccias (Tacaná)
Chiapanecan volcanic arc		Pliocene to Pleistocene	Rhyolitic to dacitic tuffs and lahars
Sierra Madre volcanic arc		Miocene	Granodiorite, quartz monzonite, granitic stocks, and andesite porphry and tuffs
Tulija	2,600	Miocene	Shales and limestone
Mompuyil, Simojovel-Yolho	950	Oligocene	Limestone, sandstone, and shale
El Bosque and Lomut	300	Paleocene to Eocene	Interbedded siltstone and fossiliferous sandstone
Lacandón-Tenejapa and Soyaló	750	Paleocene	Shale interbedded with sandstones and limestone
Sierra Madre, Angostura, Jalpabuchil	2,500	Middle to Upper Cretaceous	Limestone, dolomite, shale, and sandstone
San Ricardo	1,200–1,400	Lower Cretaceous	Anhydrite, interbedded with dolomitic limestone, some breccias, halite, and bentonitic beds
Todo Santos		Jurassic	Red beds of siltstone, sandstone, polymictic conglomerates, and andesite
Angular unconformity			
Permian Chiapas Massif		Permian	Metagranite, metagranodiorite, metadiorite
Paso Hondo		Permian	Limestone and dolomite
Groupera		Permian	Shale and limestone
Santa Rosa		Carboniferous-Permian	Phyllites, slates, shale, sandstones, and conglomerates
Chuacus		Carboniferous	Schist, phyllite, and quartzite
Unconformity			
Metamorphic complex		Proterozoic	Orthogneiss, augengneiss, migmatite marble, and amphibolite

Notes: Data compiled from Sapper (1896), Hernández-García (1973), Damon and Motesinos (1978), Sánchez-Montes De Oca (1979), García-Palomo et al. (2004), Escandón Valle et al. (2006), and García-Palomo et al. (2006); Mesozoic to Cenozoic formation names are from the Sierra de Chiapas region where Selva Negra volcanic rocks are located; formation thicknesses from García-Palomo et al. (2004), and references therein

2; Escandón Valle et al., 2006). Cenozoic volcanism in Chiapas occurred in two periods, beginning in the early Miocene with the onset of the subduction of the Cocos plate and the Sierra Madre volcanic arc. This arc formed along the Pacific coast parallel to the Middle American trench and ceased at about 9 Ma (Fig. 2; Damon and Motesinos, 1978; Meneses-Rocha, 2001). The second period of volcanic activity began at ~3 Ma with the initiation of the Chiapanecan volcanic arc, although its exact starting time remains uncertain, owing to poor quality K/Ar dates obtained from whole rocks rather

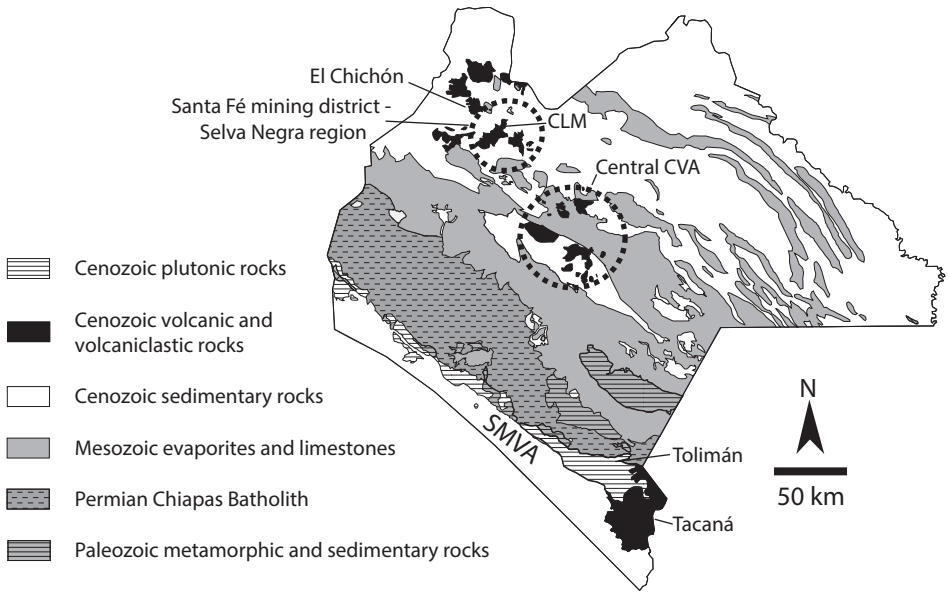

Fig. 2. Generalized geologic map of Chiapas State showing the location of the Santa Fé mining district: Selva Negra region, El Chichón, central CVA, and Tacaná volcano. Abbreviations: CLM = Cerro la Mina prospect, CVA = Chiapanecan volcanic arc, SMVA = Sierra Madre volcanic arc. Modified from geologic map of Chiapas and Tabasco State (Escandón Valle et al., 2006).

than mineral separates (e.g., Jourdan et al., 2007; Verati and Jourdan, 2014). The Chiapanecan volcanic arc is hosted in the strike-slip fault zone and is oriented 30° oblique and inland in relation to the subducting trench (Fig. 1A, B; Damon and Motesinos, 1978; Medina et al., 1990; García-Palomo et al., 2004; Mora et al., 2007).

The volcanic rocks of the central Chiapanecan volcanic arc (Fig. 2) are calc-alkaline in composition (Mora et al., 2007), whereas El Chichón and the Selva Negra volcanic rocks at the northwest end of the arc have alkaline compositions (Duffield et al., 1984; Luhr et al., 1984; García Palomo et al., 2004; Layer et al., 2009; Jansen, 2012). The Holocene El Chichón volcano, which last erupted in 1982, is an anomaly in southeastern Mexico because of its K-rich alkaline geochemistry, sulfur-rich volcanism, and isolated location (Duffield et al., 1984; Luhr et al., 1984; García-Palomo et al., 2004). The nearest Holocene volcanoes are 275 and 200 km to the southeast and northwest, respectively (Duffield et al., 1984). El Chichón is a low profile (<850 m) cluster of domes and associated pyroclastic deposits (Duffield et al., 1984).

The 1982 El Chichón volcano eruption contained primary igneous anhydrite and high sulfur content with high $\delta^{34}S$ magmatism (Luhr et al., 1984; Rose et al., 1984; Rye et al., 1984; Carroll and Rutherford, 1987; Krueger et al., 1995; Luhr and Logan, 2002; Luhr, 2008). The El Chichón eruptive products do not vary significantly in their chemical compositions, including their strong sulfur enrichment, since the volcano first started erupting 370,000 years ago (Rose et al., 1984; Layer et al., 2009). Prior to the eruption, the magma is estimated to have contained 2.6 wt % sulfur (as SO_3) with an estimated bulk magma $\delta^{34}S$ value of +4.1 to +5.8‰ (Rye et al., 1984; Luhr and Logan, 2002), which is the upper end of the range of $\delta^{34}S$ values for I-type magmas (Sasaki and Ishihara, 1979).

Selva Negra Volcanic Rocks

The Selva Negra volcanic rocks, located 20 km to the southeast of El Chichón, are host to the Cerro la Mina prospect and other Au-Ag-Cu mineralization in the district (e.g., Campamento deposit; Jansen, 2007). Selva Negra volcanic rocks cover Cretaceous carbonate rocks that are overlain by Paleogene to Neogene limestones, shales, siltstones, and sandstones (Fig. 3B). The Pliocene to Pleistocene Selva Negra volcanic rocks were first described by Damon and Motesinos (1978) as basaltic andesites, andesites, dacites, and diorites. In the Cerro la Mina region, the stratigraphic sequence is composed of lower dacite tuffs and andesite lava flows to pyroclastic breccias, andesite lava flows, dacite lapilli tuffs, and pyroclastic breccias. They are capped by coarse andesite lava flows and agglomerates, which form the resistant hill tops (Martinez Lopez, 2009). K-Ar whole-rock dating of a basaltic andesite dike, an andesite and an augite andesite, and of biotite from diorite and granodiorite yielded ages of 2.79 ± 0.08 to 1.95 ± 0.04 Ma (Fig. 3A; Damon and Motesinos, 1978). Granodiorite to diorite rocks intrude the volcanic rocks; however, in the Selva Negra region, these intrusions have been classified as monzodiorite to diorite in composition (Jansen, 2012). Two LA-ICP-MS U-Pb zircon dates from monzodiorites in the Cerro la Mina area indicate zircon crystallization at 1.06 ± 0.04 and 1.04 ± 0.04 Ma (Jansen, 2012).

Porphyry and Epithermal Mineralization in Northern Chiapas

Hydrothermal alteration and mineralization occur throughout the Selva Negra, including the Santa Fé Cu-Au mine (Fig. 3A), the Campamento Au-Ag deposit (Fig. 3B), the Cerro la Mina Au (Cu-Mo) prospect (Fig. 3B), and numerous other prospects (Pantoja, 1991; Jansen, 2007, 2012; Miranda-Gasca et al., 2009).

Cerro la Mina was first described by Miranda-Gasca et al. (2009) as a porphyry overprinted by advanced argillic alteration with average grades of 1.6 g/t Au, 7.9 g/t Ag, 0.45% Cu, and 0.18% MoS_2. The sulfides occur in veinlets along with illite, adularia, chlorite, and later calcite and rare manganocalcite alteration; extensive biotite and potassic feldspar alteration also occurs as veinlets and disseminations (Miranda-Gasca et al., 2009). An unusual feature of the prospect is that the advanced argillic alteration contains abundant hypogene halloysite-kaolinite alteration that extends to 800-m depth (Kyne et al., 2013).

The Campamento Au-Ag deposit is located 1.5 km west of the Cerro la Mina prospect (Fig. 3B). Reported measured and indicated resources are 9.37 Mt, containing 852,000 oz Au and 3.46 Moz Ag at a 1.0 g/t Au equiv cutoff (Linear Gold Corp., 2007). The deposit contains average grades of 2.8 and 11.5 g/t for gold and silver, respectively. Campamento is hosted by a sequence of Pleistocene trachyandesitic volcaniclastic rocks that have been intruded by a feldspar-phyric trachyandesite. Mineralization appears to be controlled by tightly spaced subvertical fracturing (Miranda-Gasca et al., 2009). The core of the deposit contains high-grade gold hosted in abundant narrow carbonate ± clay ± rare quartz veins that appear to be spatially associated with the feldspar-phyric trachyandesite. Highly fractured volcanic rocks in the distal zones host lower grades. The ore mineralogy consists of veins with pyrite + chalcopyrite + sphalerite + native gold ± tennantite - tetrahedrite ± galena ± acanthite ± marcasite ± several unidentified opaque phases tentatively identified as Ag-sulfosalts (A. Rainbow and K. Kyser, pers commun., 2005). The alteration consists of late, low-temperature smectite ± kaolinite that overprinted early, high-temperature biotite and muscovite (Jansen, 2007). A fluid inclusion study of the carbonate veins indicated the mineralizing fluid was of moderate temperature (261° ± 17°C) and high salinity (23 to 27 equiv wt % NaCl; J. Richards, pers commun., 2006). It was moderately oxidized with a near-neutral pH (J. Richards, pers commun., 2006).

The Santa Fé mine is located 10 km to the northeast of the Cerro la Mina prospect (Fig. 3A). This skarn deposit occurs at the contact between Oligocene limestone and a granodioritic to dioritic stock. Cu-Au-Ag mineralization is found in an extensive wollastonite halo that has a close spatial association with distinctive breccia apophyses that originate in the stock (MacCarthy, 1897; Damon et al., 1983; Pantoja, 1991; Barton et al., 1995). The calculated reserves are 10,000 t, averaging 6 g/t Au, 189 g/t Ag, and 2.46% Cu (Pantoja, 1991; Barton et al., 1995). Biotite in a mineralized diorite that intruded Oligocene limestone was dated at 2.29 ± 0.10 Ma (K-Ar) and biotite in an intermediate argillic-altered granodiorite dike yielded an age of 2.24 ± 0.08 Ma (K-Ar; Damon and Motesinos, 1978).

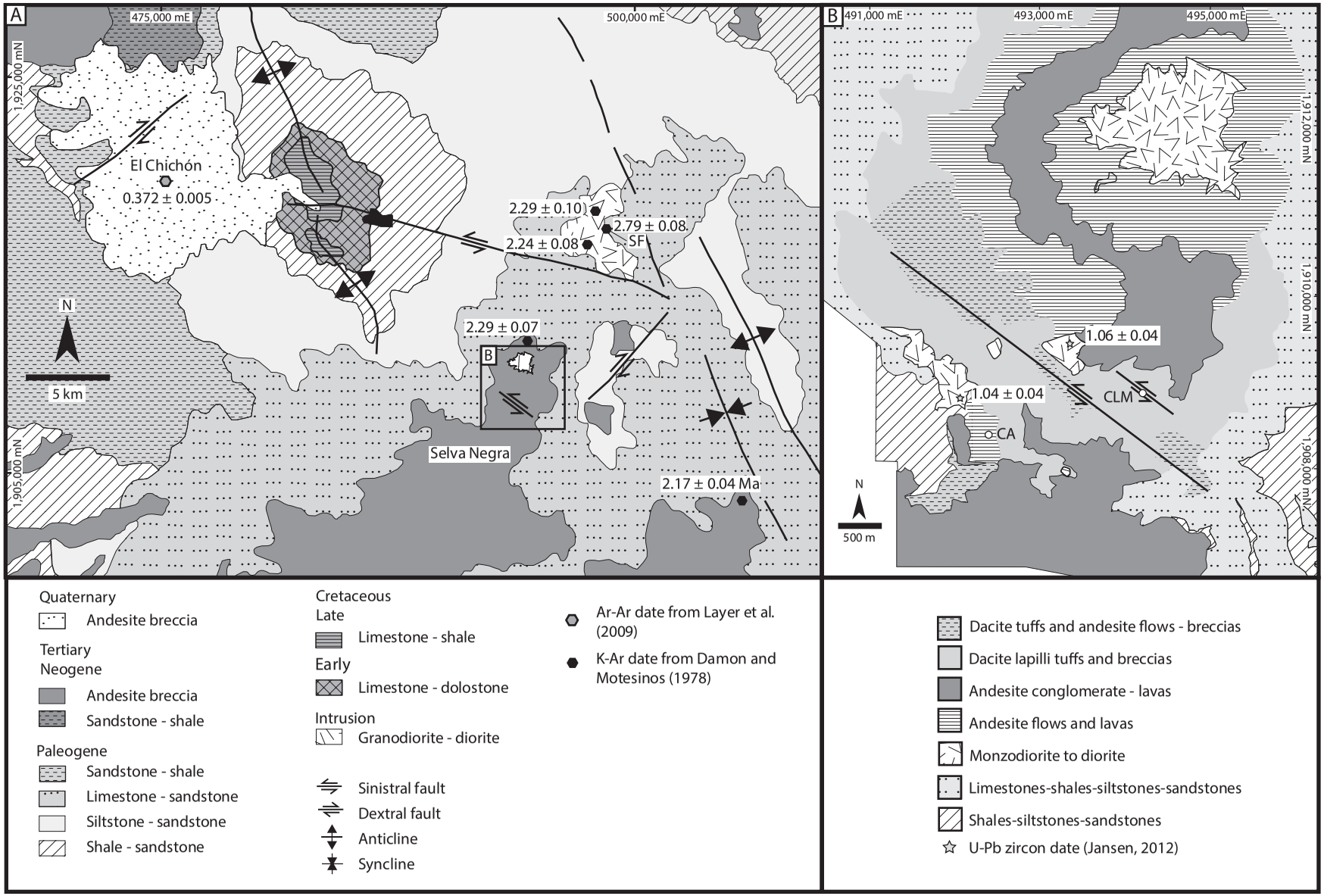

Fig. 3. Geology of northern Chiapas. A. Simplified geologic map of northern Chiapas. Modified from Islas Tenorio et al. (2005). B. Geologic map of the Selva Negra volcanic rocks. Modified after Martinez Lopez (2009). Ages in Ma. Abbreviations: CA = Campamento Au-Ag epithermal deposit, CLM = Cerro la Mina Au (Cu-Mo) porphyry-high-sulfidation prospect, SF = Santa Fé Au-Cu skarn deposit.

Prospect Geology

The Cerro la Mina volcanic succession, part of the Selva Negra volcanic package, comprises four major lithofacies based on rock textures and lithofacies associations (Table 2). The geology of Cerro la Mina has been offset by a NW-trending sinistral fault (Fig. 4A). The subvertical fault is oriented at 308° and has sinistrally offset the stratigraphy by approximately 200 m horizontally, as indicated by lithological offsets (Fig. 4A). The northeast block (Fig. 4A) preserves the lower portion of the volcanic stratigraphy with predominantly clast to matrix-supported breccias with fiamme clasts (Units 1A and B). The upper portion of the stratigraphy can be observed in the southwest block with predominantly matrix-supported conglomerates intruded by feldspar-phyric trachyandesites (Unit 3A-C). The results of logging a deep drill hole (IXCM07-28) in the southwest block indicate that the northeast block has been uplifted at least 500 m (Fig. 4B), making this a sinistral dip-slip wrench fault. A late matrix-rich granular breccia cuts the volcanic stratigraphy and is also offset by the northwest fault (Fig. 4A-B).

The lower portion of the volcanic stratigraphy predominantly contains clast to matrix-supported fragmental rocks (Units 1A-B; Figs. 4F, 5A, B) that are distinguished from other rock types by the occurrence of fiamme clasts. Units 1A and B are interbedded with thin, fine-grained volcaniclastic sandstone that locally contains pumice clasts (Unit 1C) and rare basalt (Unit 1D). Unit 1B displays eutaxitic textures but is too altered to distinguish between a welded or diagenetic compaction origin. Units 1A to C are interpreted to be a sequence of bedded pyroclastic flows. Both the upper and lower contacts of the basalt (Unit 1D) could not be observed to

Table 2. Description and Interpretation of Lithofacies for the Cerro la Mina Prospect

Unit	Lithofacies	Characteristics	Crystal/grain/lithic populations	Groundmass/ matrix	Interpretation
Unit 1A	Clast-supported breccia	Polymictic, clast-supported, with <10% fiamme clasts; normal grading	0.5–5 cm clasts that are subrounded to subangular, sparsely feldspar-phyric white-cream dacite, gray-cream mudstone, feldspar-phyric andesite	Minor	Pyroclastic flow deposit
Unit $1B_M$ Unit $1B_W$	Moderately to well-developed fiamme breccia	Polymictic, matrix-supported with 10–50% fiamme clasts	Same as above; moderately 10–30% and well-developed 30–50% fiamme clasts	1–3 mm	Pyroclastic flow deposit
Unit 1C	Volcaniclastic sandstone	Fine-grained, well sorted	Crystals are 1–2 mm, 25% in abundance, anhedral to euhedral; occasional fragments up to 3 cm of unmodified pumice, feldspar-phyric clasts and gray (lithic?) clasts		Fine-grained pyroclastic flow deposit
Unit 1D	Basalt	Fine-grained, coherent	Holocrystalline texture of plagioclase, clinopyroxene, and magnetite; occasional vesicular texture with amygdules filled with calcite, quartz, and an unidentified brown mineral	None	Basalt flow
Unit 2	Monzodiorite and diorite	Fine- to coarse-grained, equigranular, coherent	Plagioclase, clinopyroxene, biotite, magnetite, hornblende	None	Intrusion
Unit $3A_S$ Unit $3A_T$	Trachytic to square feldspar-phyric trachyandesite	Feldspar-phyric, coherent	The feldspar-phyric andesite contains 30–50% blocky to tabular feldspar phenocrysts and lesser tabular euhedral biotite, clinopyroxene, and hornblende crystals	None	Synvolcanic dome
Unit 3B	Monomictic breccia	Monomictic, blocky, clast supported, poorly sorted, and matrix poor	0.5–4 cm, subangular clasts of Unit 3A	1–2 mm	Dome autobreccia
Unit 3C	Matrix-supported conglomerate	Polymictic, poorly sorted	0.5–5.0 cm subangular clasts of predominantly aphanitic cream, with lesser feldspar-phyric and minor fine-grained lithic; rare bedding	1–2 mm	Pyroclastic or volcaniclastic debris flow
Unit 4A	Matrix-rich granule	Massive, fine-grained (<1 cm) and well sorted with clasts of Units 1 to 3	Plagioclase and potassium feldspar grains and clasts of quartz-potassium feldspar-plagioclase	<50 μm	Cerro la Mina breccia pipe core
Unit 4B	Brecciated volcanic wall rocks	Polymictic breccia	Clasts of Units 1–3; common clasts of Unit 3B (volcanic breccia clasts) and Unit 2	1–2 mm	Cerro la Mina breccia pipe rim
Unit 4C	Monomictic breccia	Monomictic, poorly sorted	0.5–2 cm, subangular clasts of monzodiorite or feldspar-phyric andesite clasts; occasional jigsaw-fit texture	1–2 mm	Cerro la Mina breccia pipe rim

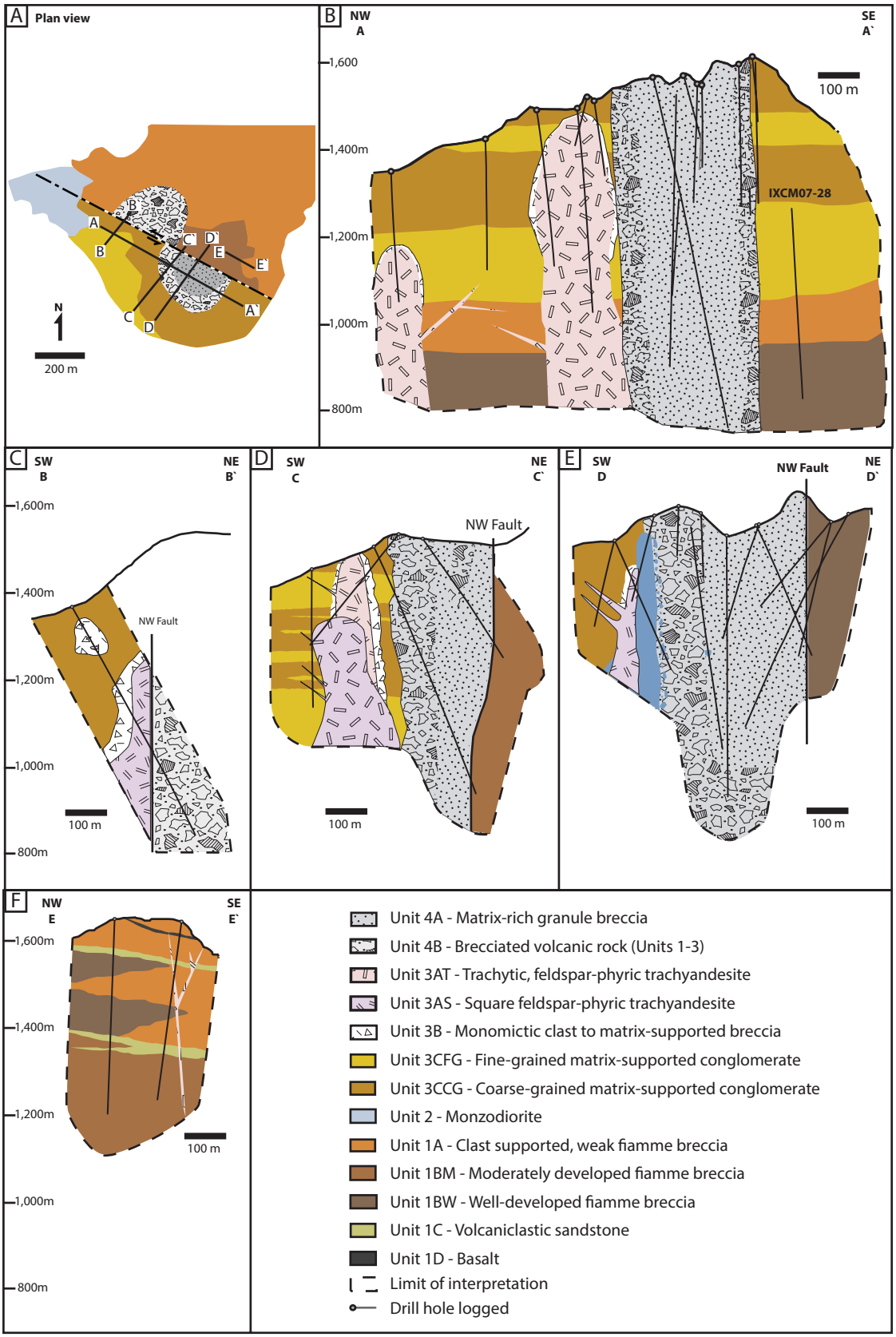

Fig. 4. Geology of the Cerro la Mina prospect shown in plan view and cross section. The geology of Cerro la Mina was logged using the graphical method of McPhie et al. (1993) on 19 drill holes at 1:100 scale, totalling 8,900 m, and 10 holes at 1:1,000 scale totalling 4,430 m.

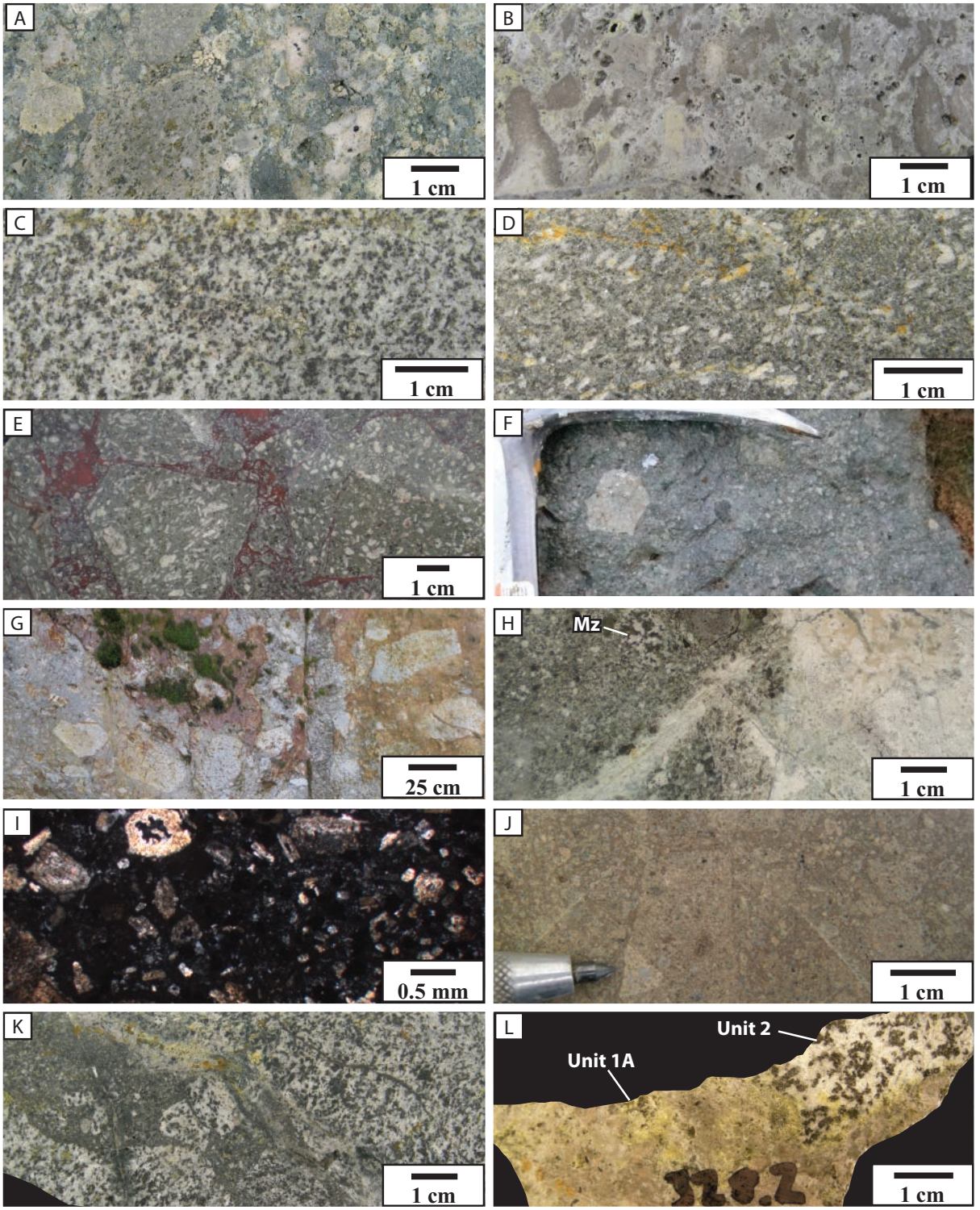

Fig. 5. Characteristics of Cerro la Mina prospect geology. A. Clast-supported breccia (Unit 1A; IXCM08-59 245.4 m). B. Fiamme breccia (Unit 1B; IXCM08-46 225.2 m). C. Coarse-grained, equigranular monzodiorite (IXCM08-55 275.3 m). D. Trachytic, feldspar trachyandesite (IXCM08-55 167.3 m). E. Hematite-cemented, monomictic breccia of feldspar-phyric trachyandesite with angular clasts (NJ08IX-500). F. Outcrop of fine-grained matrix-supported conglomerate (drill hole collar IXCM08-62). G. Outcrop of coarse-grained, matrix-supported conglomerate (drill hole collar IXCM08-63). H. Massive matrix-rich, polymict breccia cut by advanced argillic-argillic alteration (IXCM07-29 111.2 m). I. Transmitted light image of matrix-rich, polymict breccia showing fine-grained nature of rounded and angular feldspar grains (IXCM07-29 114.5 m). J. Brecciated matrix-supported breccia highlighting a clast within an angular clast (IXCM08-47 139.8 m). K. Monomictic breccia of monzodiorite (IXCM08-55 275.3 m). L. Polymictic lithic clast hosted in the breccia pipe. The lithic clast contains a clast-supported breccia (Unit 1A) in contact with monzodiorite (Unit 2; IXCM08-52 188.0 m). Mz = monzodiorite.

determine whether it is a lava, a shallow intrusion or a dome, or a cryptodome; however, we have interpreted it to be a flow based on the bedded nature of the surrounding stratigraphy. This sequence was intruded by equigranular intrusions with compositions ranging between monzodiorite and diorite (Unit 2; Figs. 4A, 5C, L; Jansen, 2012).

The pyroclastic flows are overlain by volcanic stratigraphy that is dominated by feldspar-phyric trachyandesites (Unit 3A) and matrix-supported conglomerates (Unit 3C). Narrow zones of feldspar-phyric trachyandesite (Unit 3A; Fig. 5D) cut the stratigraphy in the northeast block (Fig. 4E) and terminate as large bodies in the southwest block (Fig. 4B-E). The trachyandesite intrusions have brecciated margins of monomictic trachyandesite breccias (Unit 3B; Figs. 4B-E and 5E) that change laterally to dominant thick beds of polymictic, matrix-supported, volcanic conglomerate of mixed provenance (Unit 3C; Figs. 4A-E, 5F-G). Unit 3C is differentiated from others by the nonoccurrence of fiamme clasts and its coarse clast size.

The coarse nature, poor sorting, and large volumes of the conglomerate (Unit 3C) reflect a high supply rate of clasts and little to moderate clast abrasion. The rare gradational zones and low degree of reworking indicate that the material was probably deposited rapidly as a volcaniclastic debris flow, and is inferred to have been deposited into a graben setting similar to the nearby El Chichón volcano (García Palomo et al., 2004). The feldspar-phyric trachyandesite (Unit 3A) contains xenoliths of the earlier equigranular monzodiorite and diorite (Unit 2). These rock units are interpreted to be synvolcanic stocks and domes (Unit 3A) with autobrecciated margins (Unit 3B) that change laterally to debris and mass flows of mixed provenance (Unit 3C; Figs. 4A-E, 5F-G).

Unit 4 is a vertically oriented, cylindrical, and downward-tapering pipe. It consists of milled wall rock that is made up of a core of matrix-rich and polymitic granule (Unit 4A; Figs. 4B-E, 5H, I) and grades outward to brecciated volcanic wall rocks (Unit 4B; Fig. 5J), and rare thin (5-cm) monomictic breccia dikes (Unit 4B; Fig. 5K). Unit 4 does not have hydrothermal cement or infill and is differentiated from other rock units by the dominant fine-granule clast size represented by Unit 4A and the occurrence of fragments from the entire volcanic stratigraphy (Unit 1, Fig. 5L; Unit 3, Fig. 5J), providing evidence for its late timing. In addition, clasts of monzodiorite-diorite, only found at the bottom of the volcanic stratigraphy, were encountered in shallow locations of the breccia pipe (Fig. 5L), suggesting significant vertical transport (>600 m) occurred during the formation of this unit.

Alteration

Hydrothermal alteration at Cerro la Mina has been divided into three stages: potassic, phyllic, and advanced argillic-argillic (Table 3). The alteration stages are defined as follows: potassic alteration includes K-feldspar, quartz, and biotite; phyllic contains quartz, muscovite, illite, illite/smectite, chlorite, calcite, gypsum, and tourmaline; advanced argillic-argillic comprises quartz, dickite, pyrophyllite, alunite, kaolinite, and halloysite. All of the alteration stages form a large footprint centered on the breccia pipe and they decrease in intensity away from it (Fig. 6A).

The earliest potassic stage is defined by the vertically oriented quartz + K-feldspar ± biotite-altered core of the breccia pipe (Figs. 7A-C and 8A, D-H). The volcanic wall rocks to the breccia pipe have minor biotite ± K-feldspar alteration (Fig. 7B-E). K-feldspar in the breccia pipe is pervasive, based on the results of Na-cobaltinitrite staining (Fig. 8D). Biotite is present as small round booklets or veinlets (Fig. 8E, G) and imparts a brown color to the altered rock (Fig. 8A). A pre-breccia pipe timing for some alteration of this type is interpreted from clasts of quartz-K-feldspar that are present in the breccia pipe (Fig. 8F). However, the matrix of the breccia pipe is strongly altered to fine-grained K-feldspar, indicating a subsequent stage occurred after brecciation.

The phyllic alteration comprises a vertically oriented zone of quartz + muscovite ± illite ± tourmaline ± gypsum (likely after anhydrite) alteration centered on the breccia pipe. From the breccia pipe to the adjacent volcanic wall rocks, this alteration assemblage grades laterally outward for 2.5 km from quartz + illite ± muscovite ± tourmaline ± gypsum to illite-smectite ± smectite ± gypsum ± quartz, and finally illite-smectite + calcite + chlorite ± smectite (Figs. 6A, 7A, B, E). The pattern of this alteration around the breccia pipe is offset by a northwest fault (Fig. 6A). Laterally toward the breccia pipe, in situ spectral reflectance measurements indicate that the sericite shortwave infrared (SWIR) Al-OH peak absorption feature decreases from 2,204 to 2,192 nm and the illite crystallinity (Chang et al., 2011) increases from 0.1 to 5 (Fig. 6B). The relationship of shifts in Al-OH spectral absorption features toward shorter wavelengths in more intensely hydrothermally altered rocks has been documented in other hydrothermal deposits (Yang et al., 2011; Swayze et al., 2014). This alteration style preserves original textures and muscovite/illite-rich assemblages are gray (Fig. 8I), whereas chlorite-rich assemblages impart green colors (Fig. 8J) and overprint the potassic assemblage (Fig. 8G), with the former typically present as thick (~1-cm) gray quartz + sericite haloes along vein margins (Fig. 8A, H). Tourmaline crystals occur locally near the major northwest fault (Fig. 8K).

The advanced argillic-argillic alteration is the most completely developed at Cerro la Mina and consists primarily of quartz, halloysite 10Å ($Al_2Si_2O_5(OH)_4 \cdot 2H_2O$), halloysite 7Å ($Al_2Si_2O_5(OH)_4$), kaolinite, dickite, and minor pyrophyllite and alunite (Fig. 8B, C, L, M). The quartz is residual and always occurs with clay alteration. Siliceous zones of pure residual quartz have not been observed. This alteration has mainly affected the early-formed K-feldspar in the breccia pipe and other early alteration minerals, making the rocks gray-white (Fig. 8B, E). This alteration is restricted predominantly to the breccia pipe, but also occurs along structures associated with the northwest fault (Fig. 7E). A domain of quartz + dickite ± kaolinite ± pyrophyllite ± alunite assemblage crops out at the present-day surface, and extends to 250-m depth (Fig. 7A, B, E); below this, the alteration changes to halloysite + kaolinite, which has been recognized to at least 800-m depth (Fig. 7B, E; Kyne et al., 2013).

Advanced argillic-argillic alteration is associated with cemented breccias and veins that cut the breccia pipe; their geometry comprises two cores of breccias (Fig. 7B, E) with a change outward to veins. The upper breccia occurs over the range of ~1,450- to 1,550-m elevation, with a width and length of ~100 m and is associated with the distribution of quartz-dickite-kaolinite-pyrophyllite-alunite alteration (Fig. 7B, E).

Table 3. Summary of the Cerro la Mina Alteration Assemblages and Their Relationship to Rock Lithofacies

Classification	Potassic	Phyllic	Advanced argillic (quartz-dickite)	Advanced argillic (halloysite-kaolinite)
Mineral assemblage	K-feldspar + quartz + biotite	Quartz, muscovite, illite illite/smectite, chlorite, calcite, gypsum ± tourmaline	Quartz + dickite ± pyrophyllite ± alunite ± kaolinite	Halloysite + kaolinite
Texture	Biotite—disseminated and veinlets, K-feldspar rimming of plagioclase	Pervasive wall-rock alteration and vein haloes; muscovite and illite-rich gray, chlorite-rich green; calcite along fractures	Pervasive, gray; mosaic, jigsaw-fit, and chaotic hydrothermal breccia cement	
Location and extent	Proximal-medial	Proximal to distal	Proximal, small pod from present-day surface to 250-m depth	Proximal, to 800-m depth
Zonation	K-feldspar core, biotite distal	Quartz + muscovite core, illite/smectite + chlorite distal; tourmaline rare	None	None
Alteration style	Pervasive, vein	Pervasive, vein	Pervasive, hydrothermal breccia cement, vein	Pervasive, vein, hydrothermal breccia cement
Textural destruction	Weak to moderate	Weak to moderate	Strong	Strong
Identification	Biotite: thin section, SWIR, XRD K-feldspar: thin section, staining	SWIR, XRD	SWIR, XRD	SWIR, SEM, XRD
QXRD	25–72% K-feldspar 10–22% quartz 1–10% biotite	1–60% muscovite, illite, illite/smectite	34–36% quartz, 28–37% dickite, 5–42% pyrophyllite and 1–18% alunite	1–17.5% halloysite + kaolinite
Lithofacies				
Unit 1: Fiamme breccias	Minor	Common, pervasive, ~vein 1A – chlorite, $1B_S$ – muscovite	Rare	Rare
Unit 2: Monzodiorite to diorite	Minor, vein	Common, pervasive, ~vein	Rare	Rare
Unit 3: Trachyandesite coherent to matrix-supported conglomerate	Minor, vein	Common, pervasive, ~vein	Rare	Rare
Unit 4: Cerro la Mina breccia pipe	Common, pervasive	Common, pervasive, vein	Common, pervasive, hydrothermal breccia cement	Common, pervasive, hydrothermal breccia cement, vein

Abbreviations: QXRD = qualitative X-ray diffraction, SEM = scanning electron microscopy, SWIR = shortwave infrared spectroscopy, XRD = X-ray diffraction

The lower breccia is at ~950-m elevation, ~600 m below the upper breccia, and is approximately 100 × 100 × 100 m in size and occurs below pervasive alteration of halloysite and kaolinite (Fig. 7B, E). The upper breccia is composed of dickite + pyrite ± enargite (Fig. 8L), whereas in the lower breccia, the cement is composed of halloysite-kaolinite + marcasite + pyrite (Fig. 8M). Both breccias are zoned outward from chaotic (significant clast rotation) to mosaic (no clast rotation) textures and more distant (50 m) to veins, with the vein (Fig. 8M) mineralogy similar to the cement. The breccia clasts are angular to subangular, with the clast size ranging from a few mm to several cm. Both breccias are monomictic clasts of the breccia pipe.

Mineralization

Cerro la Mina contains disseminated fine-grained (<500 μm) sulfides, sulfosalts, and sulfates as disseminations and in veins, veinlets, and breccias cemented by advanced argillic-argillic minerals. On a broad scale, the most significant mineralization occurs in the breccia pipe (Fig. 9; Table 4) and in structures related to the NW-trending fault. The paragenesis (Table 5) comprises four stages: stage 1 (potassic alteration), stage 2 (phyllic) and stages 3 and 4 (advanced argillic-argillic alteration).

The spatial distribution of stage 1 pyrite defines an annular shape centered on the breccia pipe in plan view. In cross section, stage 1 is concentrated on the margins of the breccia pipe and extends to 200 m below the present surface and 200 m away from the breccia pipe (Fig. 10B, D, E). Stage 1 pyrite grains occur only in early quartz + K-feldspar ± biotite veins; this pyrite is typically 50 to 200 μm, hosts no inclusions, and has been fractured into a jigsaw-fit breccia texture (Fig. 11A).

Disseminated stage 2 pyrite, chalcopyrite, and molybdenite are centered on the breccia pipe, spatially associated

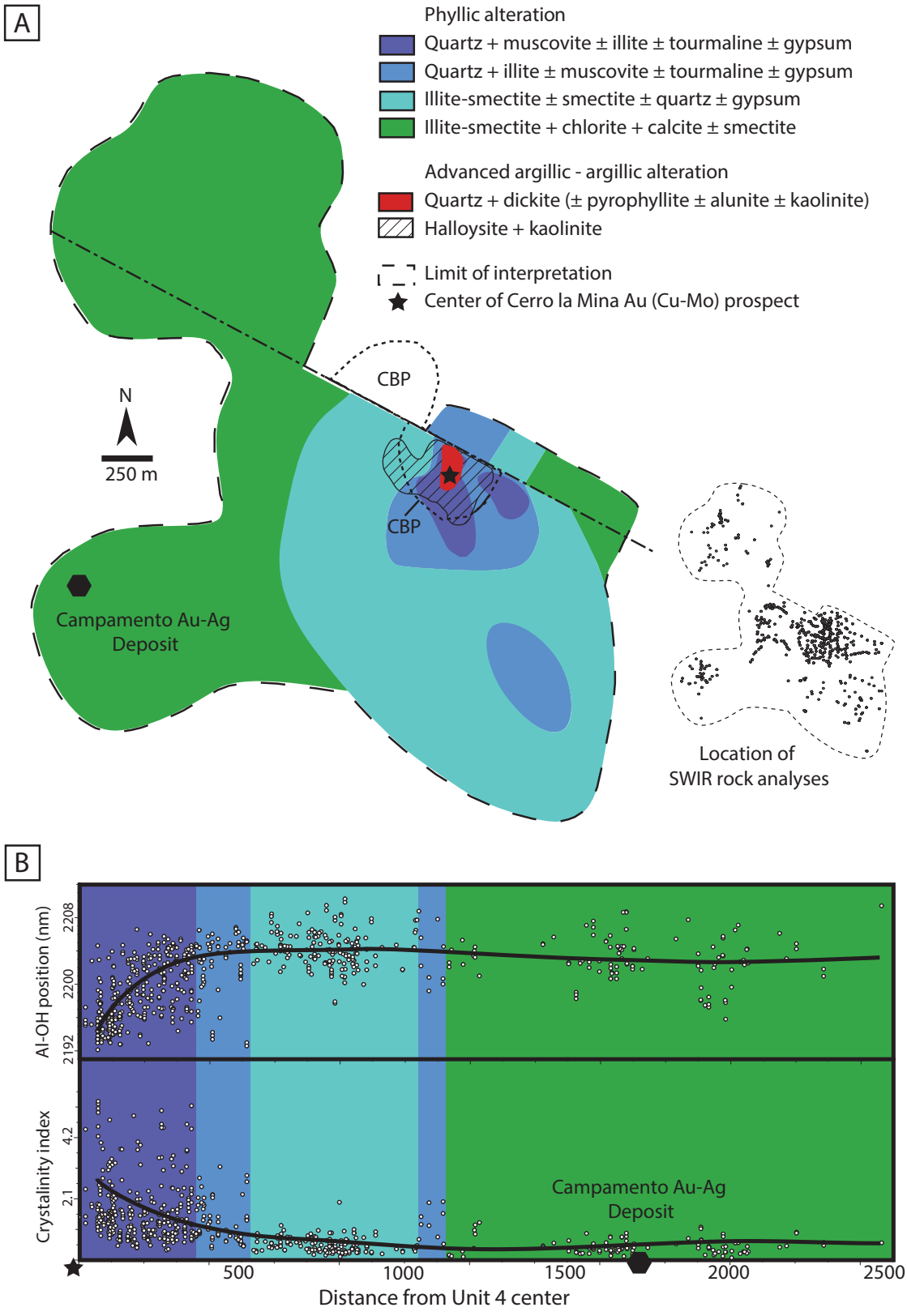

Fig. 6. Cerro la Mina surface alteration. A. The phyllic and advanced argillic-argillic alteration show a concentric pattern centered on the breccia pipe. The northwest fault has offset the alteration zonation pattern. B. Crystallinity and Al-OH zonation of phyllic alteration versus distance from the center of the breccia pipe. SWIR analyses collected using a TerraSpec ASD spectrometer and TSG™ Pro version 5 during this study and by Brigus Gold. Abbreviation: CBP = Cerro la Mina breccia pipe.

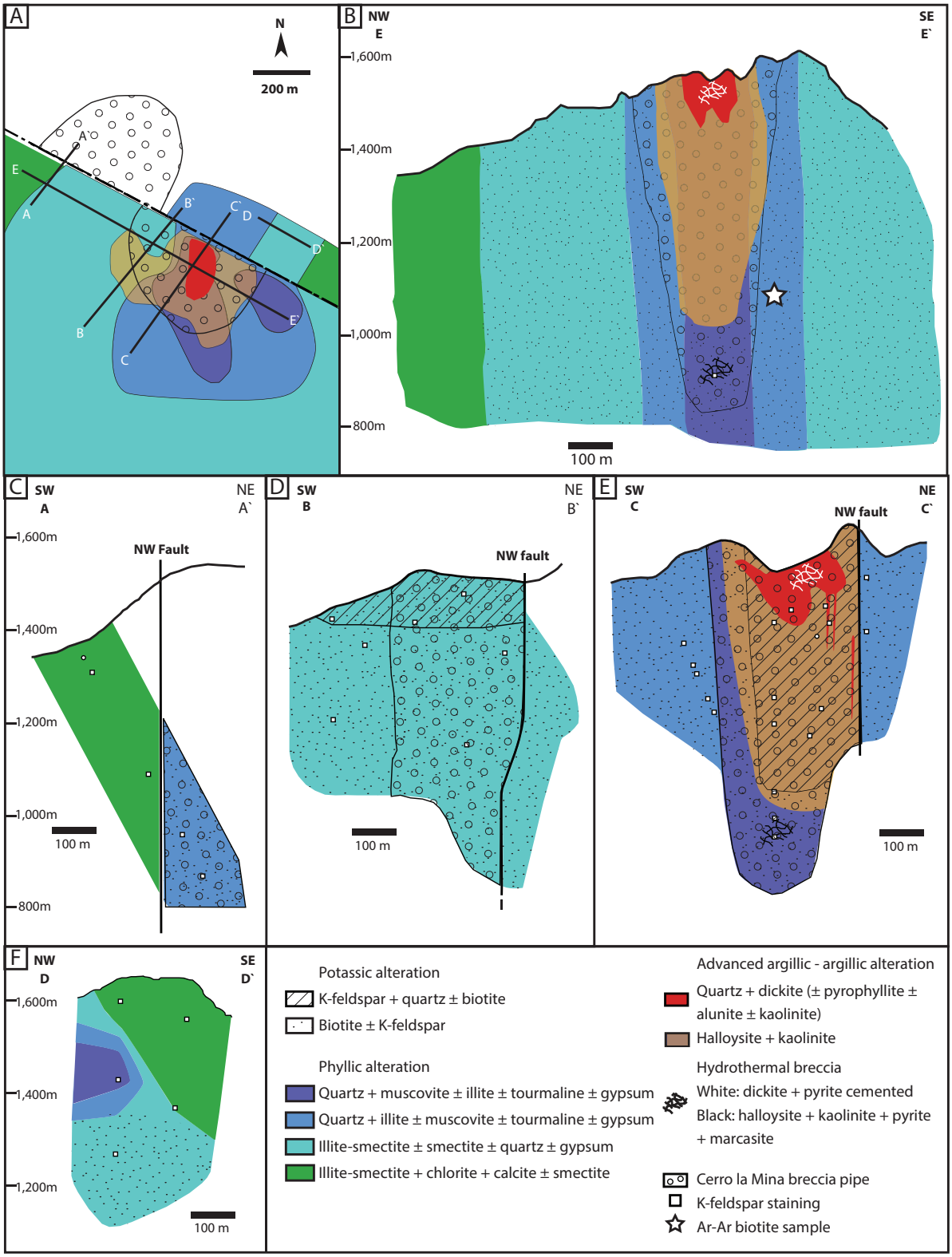

Fig. 7. Alteration of the Cerro la Mina prospect, shown in plan view and cross section. Drill hole logging constraints as per Figure 6. SWIR spectral analyses of ~2,000 drill core and surface samples were obtained using a TerraSpec ASD spectrometer Spectral interpretation and feature extraction of spectra previously collected by Brigus Gold geologists and spectra during our study was done using the software TSG™ Pro version 5. X-ray diffraction (XRD) analysis from Kyne et al. (2013) and 20 samples were analyzed at the University of Ballarat, Australia, using Siemens D500 and D501 diffractometers with Fe-filtered CoK_α radiation. Forty-three samples were stained for the occurrence of K-feldspar following the methods described in Bailey and Stevens (1960).

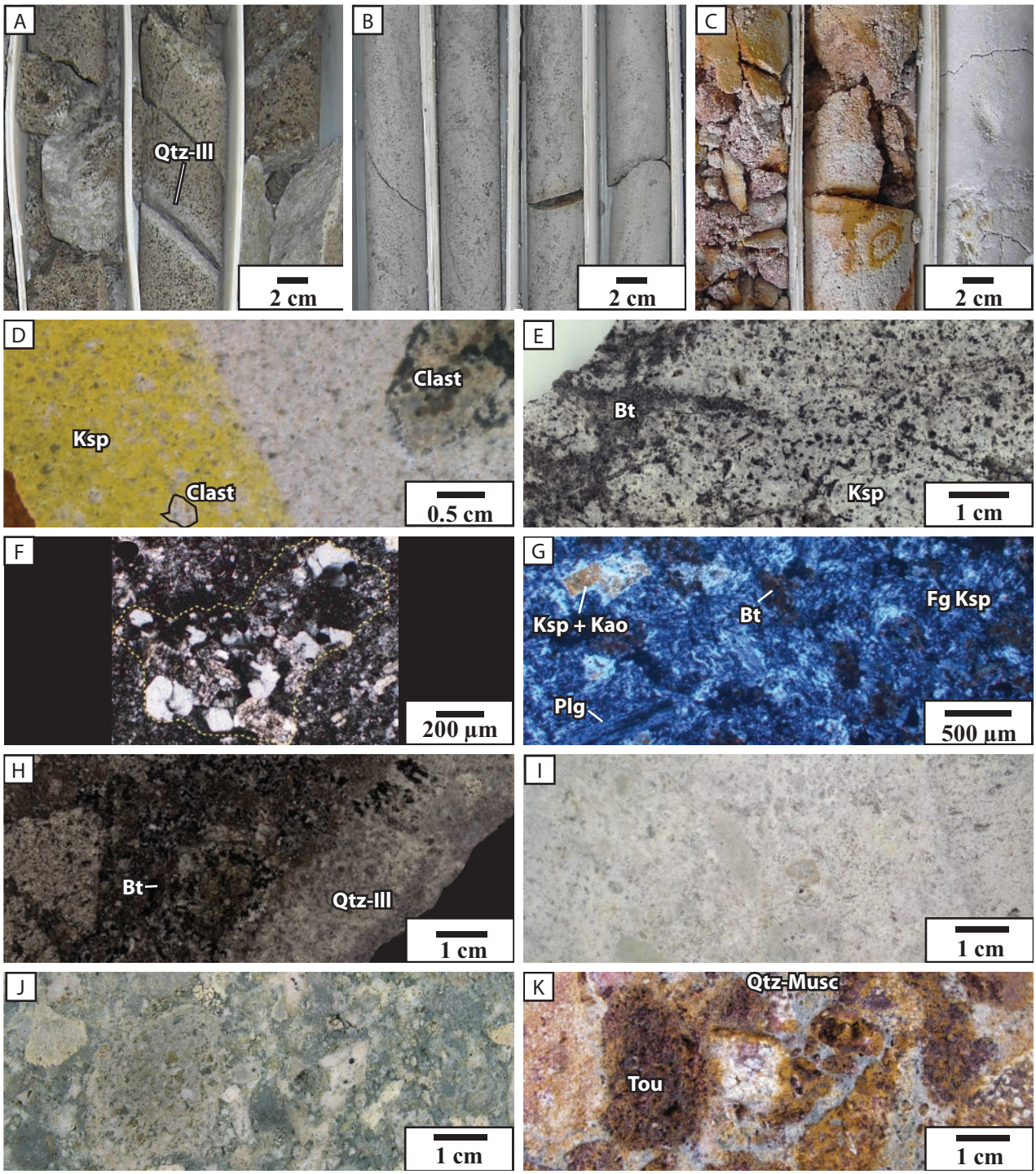

Fig. 8. Cerro la Mina alteration. A. Quartz-biotite cut by quartz-illite alteration (IXCM07-28 459.9–462.0 m). B. Halloysite-kaolinite alteration (IXCM07-44 43.0–45.10 m). C. Oxidized quartz-dickite-pyrophyllite-alunite-kaolinite alteration (IXCM06-10 256.2–259.6 m). D. Matrix-rich breccia (Cerro la Mina breccia pipe) with Na-cobaltinitrite staining highlighting K-feldspar alteration of matrix and clast outlines (IXCM08-61 439.0 m). E. Veinlets and booklets of biotite with K-feldspar (IXCM07-25.6.10.3 m). F. Clast of quartz-K-feldspar in the breccia pipe (IXCM06-16.313.0 m). G. Cross polarized image showing a biotite veinlet and abundant fine-grained K-feldspar and K-feldspar replacement of plagioclase. K-feldspar has been partially replaced by kaolinite (IXCM07-25 589.3 m). H. Gray, quartz-illite alteration occurring on vein margin cutting biotite alteration (IXCM07-28 487.4 m). I. Gray quartz-illite alteration of a fiamme breccia (IXCM07-23 233.5 m). J. Green illite-smectite + chlorite alteration of a clast-supported breccia (IXCM08-47 65.1 m). K. Oxidized brown tourmaline crystals altering clasts with a quartz-muscovite altered matrix (IXCM08-59 245.5 m).

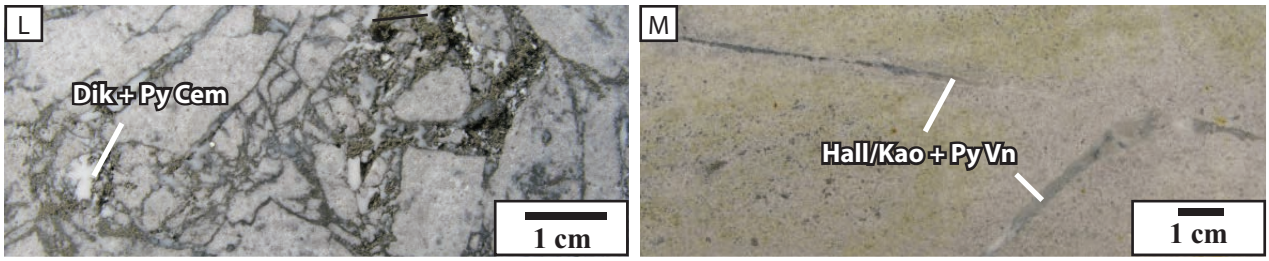

Fig. 8. *(Cont.)* L. Jigsaw-fit dickite + pyrite cemented hydrothermal breccia (IXCM08-47 238.4 m). M. Halloysite-kaolinite vein (IXCM08-51 109.5 m). Abbreviations: Bt = biotite, Cem = cement, Dik = dickite, Fg = fine-grained, Hall = halloysite, Ill = illite, Kao = kaolinite, Ksp = K-feldspar, Musc = muscovite, Plg = plagioclase, Py = pyrite, Qtz = quartz, Ser = sericite, Tou = tourmaline, Vn = vein.

with phyllic alteration. There is a vertical and lateral zonation of stage 2 sulfides from chalcopyrite + molybdenite + pyrite associated with quartz + muscovite alteration in the core that changes outward to pyrite ± chalcopyrite associated with quartz + illite alteration (Fig. 10A, B, E). Stage 2 pyrite (Fig. 11B) is the most abundant sulfide in the volcanic rocks distal to the breccia pipe; it is associated with illite-smectite alteration (Fig. 10A, B). Stage 2 sulfides range from 25 to 500 μm in size and occur in veins or disseminations (Fig. 11B, C). The pyrite and chalcopyrite are typically intergrown and are strongly embayed with irregular edges, suggesting these minerals were not in equilibrium with later fluids. Stage 2 pyrite contains numerous inclusions, predominantly of clay and rutile with lesser pyrrhotite and chalcopyrite (Fig. 11B). Molybdenite forms long,

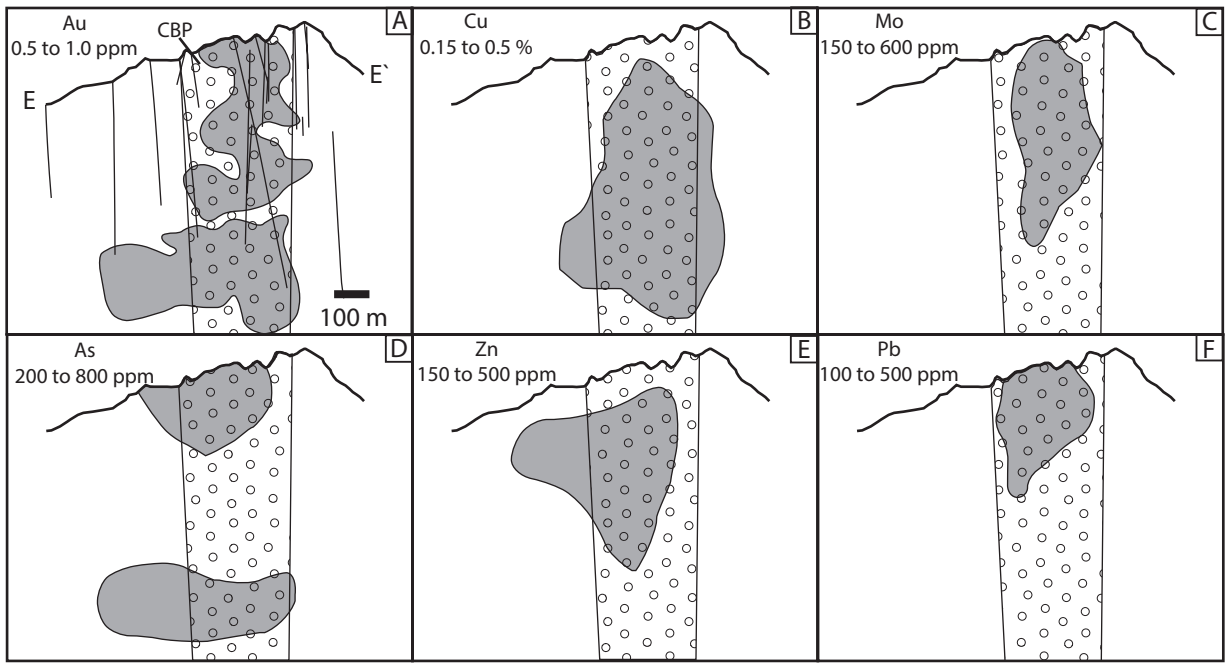

Fig. 9. Zonation of Au, Cu, Mo, As, Zn and Pb at the Cerro la Mina prospect in relationship to the breccia pipe. Long section E-E' location shown in Figure 8. Light gray is the outline of the breccia pipe and the dark gray fill shows the distribution of the respective element. Compiled from company data consisting of 2-m interval sampling, Au 50-g fire assay with atomic absorption finish and 35 element aqua regia digestion ICP-MS. CBP = Cerro la Mina breccia pipe (Unit 4).

Table 4. Comparison of Au-Cu-Mo Grades for the Breccia Pipe, Volcanic Wall Rocks (Units 1 to 3) and Quartz-Dickite Alteration

Rock type/alteration	No. of analyses	Au g/t Mean (range)	Cu % Mean (range)	Mo ppm Mean (range)
Breccia pipe (Unit 4)	4,657	0.4 (0–87.7)	0.16 (0–4.2)	131 (0.5–4,800)
Volcanic wall rocks (Units 1–3)	2,525	0.1 (0–4.1)	0.03 (0–1.1)	12 (0–615)
Quartz-dickite alteration	160	0.7 (0.1–5.0)	0.23 (0–11.6)	345 (11–4,230)

Notes: Compiled from company data consisting of 2-m interval sampling, Au 50-g fire assay with atomic absorption finish, and 35-element aqua regia digestion ICP-MS

Table 5. Summary of the Cerro la Mina Mineralization and Their Relationship to Alteration and Rock Lithofacies

Stage	1	2	3	4
Mineral assemblage	Py	Py + Cpy + Mo	Mc + Sph + Ga + Ba	Py + En + Cv
Grain size	50–200 μm	25–500 μm	Mc 50–200 μm; Sph, Ga, Ba 50–1,000 μm	Py and En 5–300 μm Cv <50 μm
Texture	Jigsaw fit, rare Au inclusions	Py, Cpy and Mo are irregular and embayed; Py has inclusions of clay, Rt, pyrophyllite, Cpy, Bn, and Mo	Marcasite forms frayed, concentric rims, wispy, or long slender crystal shapes; Sph + Ga + Ba are rare and commonly intergrown in veins	Py has 40% inclusions, commonly intergrown with en or forming fine concentric rims on early Py; Cv forms in the fractures of Cpy; Cv and En form complex intergrowths
Timing	Infills quartz–K-feldspar-biotite veins	Rimming stage 1	Banded rims on stage 1 and 2	Observed rimming stage 1, 2, and 3; En + Py + Cv replacing Cpy
Occurrence	Vein and dis	Vein and dis	Vein, hbx, and dis	Vein, hbx, and dis
Zonation	None	IrPy + Cpy + Mo core surrounded by IrPy	Coarser-grained in quartz-dickite; fine-grained in halloysite-kaolinite	Coarser-grained in quartz-dickite; fine-grained in halloysite-kaolinite
Associated alteration	Early phyllic	Late phyllic	Advanced argillic	Advanced argillic
Associated lithofacies	Units 1-3	Cpy + Mo in Unit 1 Py in Units 1–4	Predominantly in Unit 1 and rarely in Units 1–3	Predominantly in Unit 1 and rarely in Units 1–3

Abbreviations: Ba = barite, Bn = bornite, Cpy = chalcopyrite, Cv = covellite, dis = disseminations, En = enargite, Ga = galena, hbx = hydrothermal breccia, Mc = marcasite, Mo = molybdenite, Py = pyrite, Sph = sphalerite

stubby booklets or slender needles depending on the orientation of the crystal axis. Molybdenite is associated with the distribution of chalcopyrite and pyrite but is not intergrown.

Stages 3 and 4 are associated with advanced argillic-argillic alteration and their distribution (Fig. 10B) correlates with the distribution of Au (Fig. 9). Stage 3 mineralization is vertically oriented, coincident with the breccia pipe, and is comprised of fine-grained (<100 μm) marcasite, sphalerite, galena, and barite (Fig. 10A, B, D, E). Stage 3 sulfides occur only in low abundances, with Zn and Pb concentrations of less than 500 ppm. These sulfides are found as disseminations in veins and hydrothermal breccia cement associated with advanced argillic-argillic alteration. Where acid-etched, the marcasite displays fine growth bands on the edges of stage 2 chalcopyrite and pyrite grains (Fig. 11D). Sphalerite has overgrown chalcopyrite with concentric rims in halloysite-kaolinite veins (Fig. 10E). Locally, intergrown coarse-grained barite (1 cm long and 0.25 cm wide), sphalerite (200 μm), and galena (300 μm) occur in halloysite-kaolinite veins (Fig. 11F).

Stage 4 contains predominantly arsenian pyrite with minor enargite and covellite that occur in advanced argillic-cemented breccias and veins. Dickite + pyrite ± enargite-cemented breccias host the highest average grades of 0.7 g/t Au and 0.23% Cu (Table 4). The arsenian pyrite has ragged textures (Fig. 11G) and occurs as rims around other sulfides (Fig. 11D, H) or as rare, fine-grained crystals. Enargite is commonly associated with arsenian pyrite and locally with chalcopyrite, as fine-grained crystals within and on the rim of chalcopyrite (Fig. 11A). Covellite is rare, occurring in fractures and rims around chalcopyrite (Fig. 11I), and is locally intergrown with enargite.

Stage 4 is distributed in two distinct zones, defined here as the upper and lower arsenic-rich zones, that are spatially associated with the breccias cemented by advanced argillic-argillic alteration (Figs. 9, 10A, B, E). The upper arsenic-rich zone occurs from present-day surface to 200-m depth, forming a bowl-shaped zone that contains pyrite grains + pyrite rims + enargite ± covellite. The lower arsenic-rich zone contains pyrite rims ± enargite ± covellite and occurs below 1,100-m elevation (> 600 m below the surface) forming a subhorizontal zone (Figs. 9, 10B, E). Minor, fine-grained pyrite ± covellite occur between the upper and lower arsenic-rich zones.

The near-surface supergene oxidized zone extends on average to 50 m below the present surface, with a maximum depth of 175 m (Fig. 10B-F). Partial oxidation, where pyrite and oxides occur together, persists locally to depths of 545 m below the surface along narrow fractures (<1 m) associated with the northwest fault. The oxide zone contains supergene halloysite, kaolinite, opal, goethite, hematite, and barite. Relict quartz-dickite-pyrite-enargite alteration in the oxide zone (Fig. 10B, E) has high Au/Cu ratios, resulting from the breakdown of sulfides.

Vein Paragenesis

Veins are poorly preserved in drill core from Cerro la Mina owing to the highly fractured nature of the core. Where preserved, the core predominantly contains veinlets or veinlet stockworks, with only rare veins greater than 1 cm in width. Stage 1 pyrite veins infilled early potassic veins; these have been brecciated in situ (Fig. 12C, D), consistent with a pre-breccia pipe timing for the early potassic alteration and stage 1 pyrite. The potassic veins and stage 1 pyrite vein have been cut by stage 2 pyrite veins with phyllic-altered halos (Fig. 12A, B). Stage 3 halloysite + kaolinite + marcasite + sphalerite veins infilled stage 2 illite + chalcopyrite + pyrite + molybdenite veins (Fig. 12E, F). A halloysite-kaolinite vein with sphalerite-barite-galena bands suggests multiple alteration episodes (Fig. 12G, H).

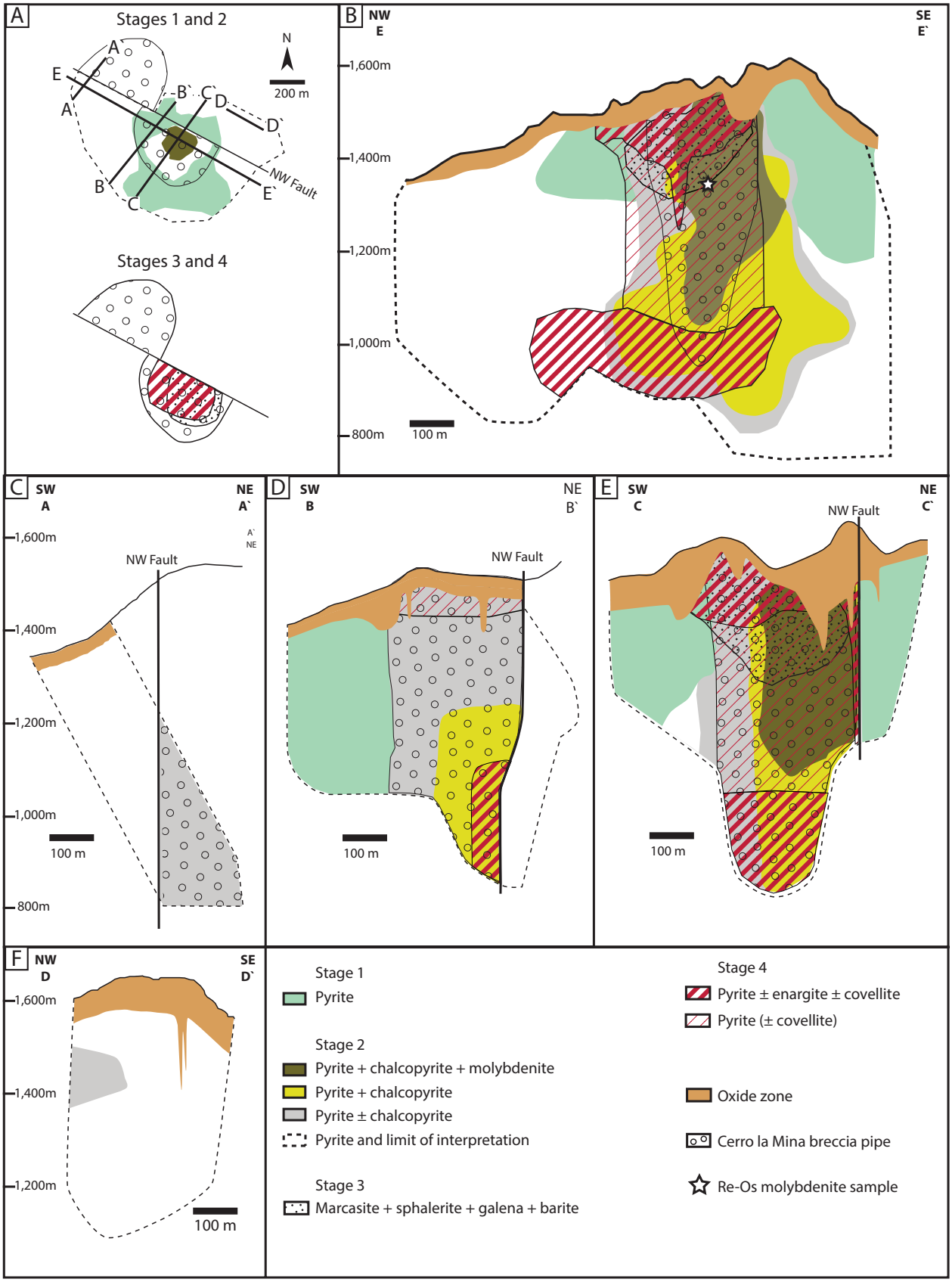

Fig. 10. Distribution of mineralization stages in the Cerro la Mina prospect. A. Plan view. B-F. Cross sections with locations shown in A. Drill hole logging constraints as per Figure 6.

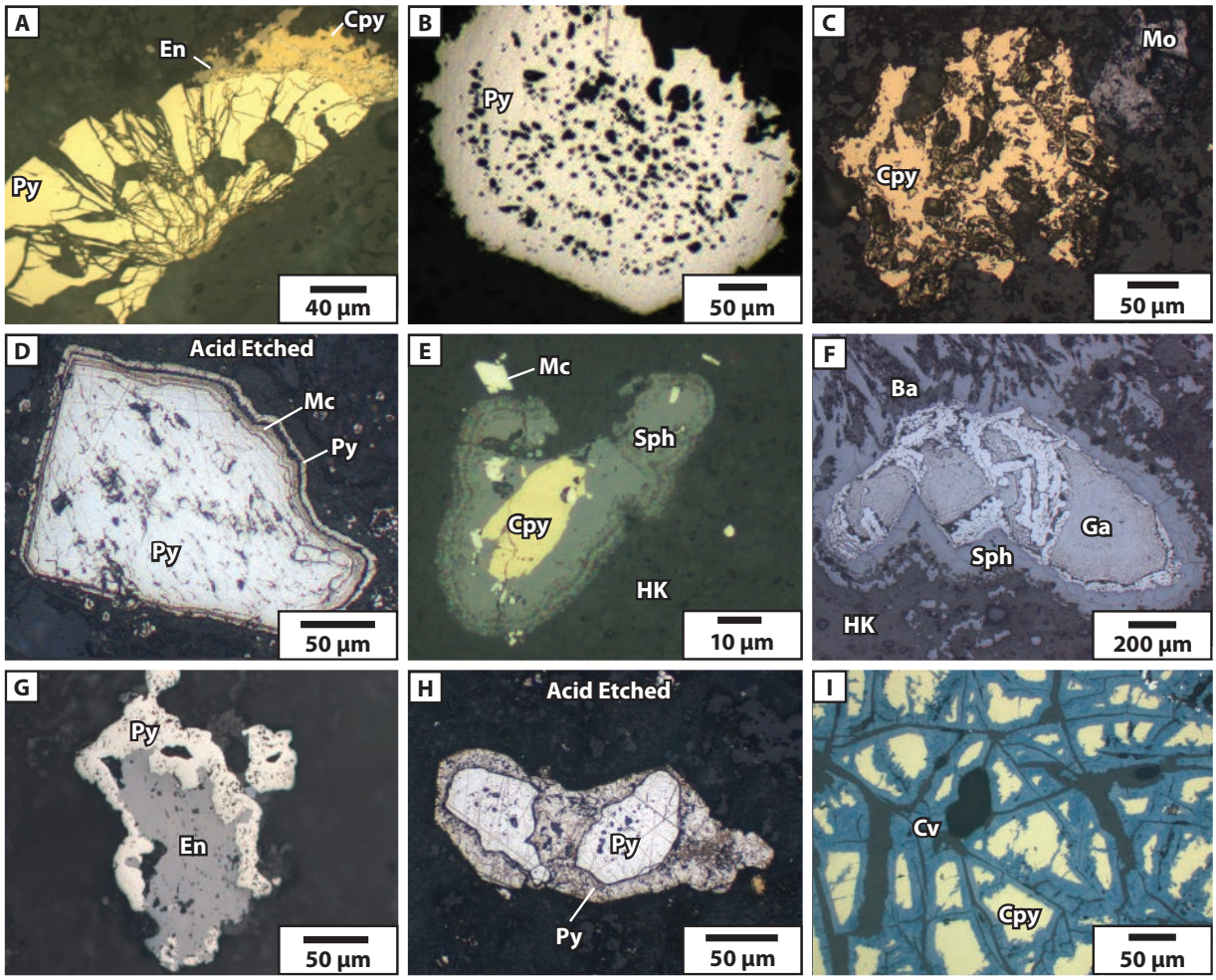

Fig. 11. Characteristics of stages 1 and 2 mineralization (A-C), stage 3 (D-F), and stage 4 (G-I). A. Stage 1 pyrite with a fractured texture rimmed by chalcopyrite (stage 2). The chalcopyrite has been partially replaced by enargite (stage 4)(IXCM06-16.313.4 m) B. Stage 2 pyrite with abundant inclusions displaying a concentric pattern and cuspate edges (IXCM08-63 489.4 m). C. Stage 2 chalcopyrite with strongly irregular and cuspate edges and ratty molybdenite (stage 2) (IXCM08-51 285.6 m). D. Stage 3 marcasite and stage 4 pyrite forming concentric bands on stage 2 pyrite highlighted by acid etching (IXCM08-48 130.3 m). E. Concentric rims of stage 3 sphalerite around a stage 2 chalcopyrite in a halloysite-kaolinite vein (IXCM06-09 214.9 m). F. Intergrown stage 3 barite, galena, and sphalerite in a halloysite + kaolinite vein (IXCM087-51 478.2 m). G. Enargite (stage 4) intergrown with stage 4 pyrite (IXCM06-09 86.3 m). H. A thick 30-μm stage 4 pyrite rim encasing stage 2 pyrite, as highlighted by nitric acid etching (IXCM06-09 100.7 m). I. Covellite (stage 4) developed along fractures of chalcopyrite (stage 2) (IXCM08-48 130.3 m). Abbreviations: Ba = barite, Cpy = chalcopyrite, Cv = covellite, En = enargite, Ga = galena, HK = halloysite + kaolinite, Mo = molybdenite, Mc = marcasite, Py = pyrite, Sph = sphalerite. Pyrite and marcasite were acid etched using a 70% water/HNO_3 mixture placed on a polished slab or polished mount for 5 to 20 s to allow for the observation of arsenic-rich zones in pyrite.

Rare hydrous and anhydrous phosphate minerals were observed in veins, including planerite $(Al_6(PO_4)_2(PO_3OH)_2(OH)_8 \cdot 4(H_2O)$, vivianite $(Fe^{2+}{}_3(PO_4)_2 \cdot 8(H_2O)$, trolleite $(Al_4(PO_4)_3(OH)_3$, and berlinite $(AlPO_4)$ (Fig. 12I, J). The phosphates occur in veins that cut early stage 1 and 2 veins and occur distal to advanced argillic-argillic alteration. The timing of phosphate mineralization with respect to advanced argillic-argillic alteration is unclear.

Geochronology

Re-Os results

Re-Os dating of a stage 2 molybdenite sample indicates that (location shown in Fig. 10B; results in App. 2) Re and Os concentrations were 691.6 ppm and 5.651 ppb, respectively, and an Re/Os model age of 780 ± 10 ka (2σ) was obtained. This age represents the timing of stage 2 Cu-Mo mineralization, associated with phyllic alteration.

$^{40}Ar/^{39}Ar$ results

$^{40}Ar/^{39}Ar$ dating of a hydrothermal biotite sample (location shown in Fig. 7B; App. 1) yielded a plateau age of 689 ± 13 ka (2σ) including 96% of the released ^{39}Ar (MSWD = 0.86; P = 0.60). The steps are concordant within uncertainty (Fig. 13). The plateau age conforms well to that expected from a sample that remained thermally undisturbed since crystallization and relatively rapid cooling. The age spectrum also does not show any disturbance from excess argon.

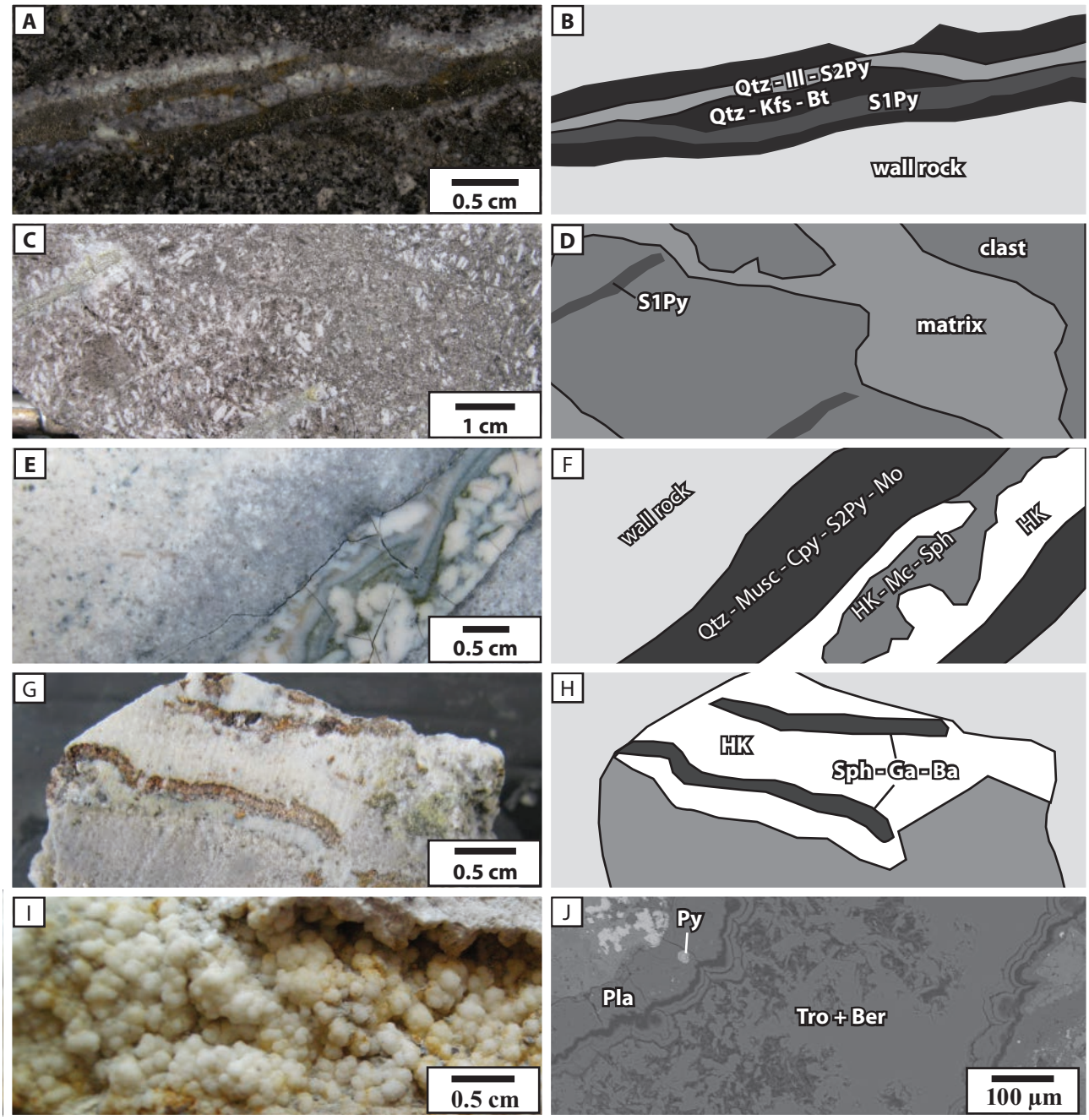

Fig. 12. Vein textures of Cerro la Mina. A/B. A Stage 1 pyrite vein has infilled an early quartz–K-feldspar–biotite veins, which have been cut by an illite + stage 2 pyrite vein. (IXCM08-55 226.5 m). C/D. Truncated stage 1 pyrite veins in a clast from the breccia pipe (IXCM08-52 188.0 m). E/F. Early phyllic alteration associated with a dark gray stage 2 quartz + muscovite + chalcopyrite + pyrite + molybdenite vein infilled with a stage 4 halloysite-kaolinite + marcasite + sphalerite vein (IXCM06-09 214.9 m). G/H. Vein with alternating bands of halloysite + kaolinite and stage 3 sphalerite + galena + barite (IXCM08-51 478.2 m). I. Botryoidal planerite occurring in a vein (IXCM08-45 64.9 m). J. Backscattered image of vein shown in I. Abbreviations: Ba = barite, Ber = berlinite, Bt = biotite, Cpy = chalcopyrite, Ga = galena, HK = halloysite + kaolinite, Ill = illite, Kfs = K-feldspar, Mc = marcasite, Mo = molybdenite, Musc = muscovite, Pla = planerite, Py = pyrite, Qtz = quartz, S = stage, Sph = sphalerite, Tro = trolleite.

The inverse isochron plot yielded the same age of 0.682 ± 0.027 Ma and shows a high degree of concordancy among all the 15 heating steps (MSWD = 0.89; P = 0.56) with all but one step plotting within ± 2σ. The $^{40}Ar/^{36}Ar$ intercept shows a value of 302 ± 5 Ma, indistinguishable from the air ratio of 298.6 ± 0.1 Ma from Lee et al. (2006), demonstrating that no excess $^{40}Ar^{*}$ is present in the biotite. The age of 689 ± 13 ka is taken to be the age at which the hydrothermal biotite cooled below its closure temperature of ~300ºC (Harrison et al., 1985).

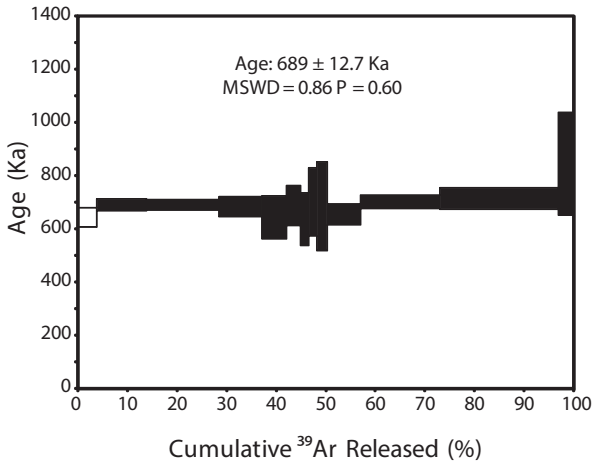

Fig. 13. $^{40}Ar/^{39}Ar$ age spectrum plot of Cerro la Mina hydrothermal biotite. The flat spectrum is typical of a sample that remained thermally undisturbed since crystallization. Black segments are included in the plateau age calculations. The biotite was irradiated for 2 h in the Hamilton McMaster University nuclear reactor (Canada). The $^{40}Ar/^{39}Ar$ analyses were performed at the Western Australian Argon Isotope Facility at Curtin University. The sample was step-heated in a double vacuum high-frequency Pond Engineering© furnace. The gas was purified in a stainless steel extraction line using two AP10 and one GP50 SAES getters and a liquid nitrogen condensation trap. Ar isotopes were measured in static mode using a MAP 215-50 mass spectrometer (resolution of ~400; sensitivity of 4×10^{-14} mol/V) with a Balzers SEV 217 electron multiplier mostly using 9 to 10 cycles of peak-hopping. Sample ID: IXCM07-25 589.3.

Sulfur Isotopes

Samples were taken from various stages of the paragenesis and at various distances from the core of the deposit to analyze for sulfur isotope composition. Results for 21 ^{34}S analyses on stage 1 pyrite, stage 2 chalcopyrite and pyrite, stage 3 barite, and stage 4 pyrite are presented in Table 6. Marcasite, sphalerite, and galena proved to be too fine grained to obtain a pure sample. To test the natural variation in the sulfur value of multiple sulfide grains from the same sample, five separate samples of stage 2 pyrite were microdrilled from sample IXCM08-62 300.1. The sulfur values varied ±0.6‰ (2σ).

The $\delta^{34}S$ values for the Cerro la Mina sulfides range from –2.5 to +4.9‰ with a mean of +0.7‰ (Fig. 14). Stage 1 has two populations at approximately –2.5 and +2.0‰, with values ranging from –2.5 to +2.2‰ and a mean of +0.2‰ (Fig. 14). Stage 2 $\delta^{34}S$ ranges from –0.5 to +0.9‰ with a mean of +0.3‰ (Fig. 14). One sample of barite from stage 3 has a $\delta^{34}S$ of +10.5‰. The $\delta^{34}S$ of stage 4 is slightly higher, between +1.1 and +4.9‰, with a mean of +2.3‰ (Fig. 14). Stage 2 has the widest sample distribution and did not show any consistent spatial vertical or horizontal changes in $\delta^{34}S$ (Fig. 14). Samples analyzed for stages 1, 3, and 4 do not have sufficient spatial coverage to allow spatial trends to be detected (Fig. 14). No sulfides were observed in equilibrium with barite, preventing sulfide/sulfate geothermometry.

Discussion

Geology

The Cerro la Mina stratigraphy contains pyroclastic flow deposits with rare basalt, synvolcanic domes, debris and mass flows, and the breccia pipe. With the exception of the breccia pipe, the lithofacies at Cerro la Mina are similar to those produced by regional volcanism in the Chiapanecan volcanic arc, where low profile (<850-m high), small-volume (3–4 km^3)

Table 6. $\delta^{34}S$ Data for Sulfates and Sulfates from the Four Stages of Mineralization

Sample no.	Stage	Mineral	Weight (mg)	Yield (mmHg)	$\delta^{34}S$ CDT (‰)
IXCM07-21 281.0	1	Pyrite	13.7	16.8	+1.8
IXCM07-27 97.5	1	Pyrite	12.4	24.8	+1.9
IXCM08-48 130.3	1	Pyrite	13.0	17.6	–2.4
IXCM08-55 225.6	1	Pyrite	13.8	20.4	+2.2
IXCM08-56 68.5	1	Pyrite	13.8	22.2	–2.5
IXCM06-09 136.9	2	Chalcopyrite	79.8	37.0	+0.4
IXCM07-20 798.4	2	Chalcopyrite	98.2	53.0	–0.5
IXCM06-16 528.3	2	Pyrite	11.7	21.0	+0.7
IXCM07-28 487.4	2	Pyrite	12.0	12.4	–0.4
IXCM08-45 42.9	2	Pyrite	16.2	22.4	+0.8
IXCM08-62 182.2	2	Pyrite	21.9	17.0	+0.4
IXCM08-63 300.1 #1	2	Pyrite	16.2	23.6	+0.5
IXCM08-63 300.1 #2	2	Pyrite	13.1	29.0	+0.1
IXCM08-63 300.1 #3	2	Pyrite	13.6	17.6	+0.7
IXCM08-63 300.1 #4	2	Pyrite	12.7	15.4	+0.9
IXCM08-63 300.1 #5	2	Pyrite	24.2	30.8	+0.6
IXCM07-21 284.3	3	Barite	54.3	30.0	+10.5
IXCM08-47 238.4	4	Pyrite	1.6	2.2*	+1.7
IXCM08-51 44.8	4	Pyrite	10.3	8.8	+4.9
IXCM06-09 100.7	4	Pyrite	4.9	4.8*	+1.1
IXCM06-09 106.8	4	Pyrite	16.4	29.0	+1.6

Notes: The $\delta^{34}S$ values for sulfide and sulfate samples were analyzed at the Central Science Laboratory, University of Tasmania on the VG SIRA series II mass spectrometer; SO_2 was extracted from sulfides and sulfates using methods described in Robinson and Kusakabe (1975) and Yanagisawa and Sakai (1983); A cold finger was used (*) when the yield was below 5 mm Hg; in-house standards were used and calculated against International Atomic Energy Agency (IAEA) standards to ±0.1‰; the in-house sulfide standards included galena from Broken Hill and Rosebery with $\delta^{34}S$ values of +3.0 and +12.4‰, respectively (Huston et al., 1995); in-house sulfate standards included barite from the Madame Howard deposit and seawater sulfate (Tasul I) with $\delta^{34}S$ values of +31.2 and +20.9‰, respectively (Huston et al., 1995)

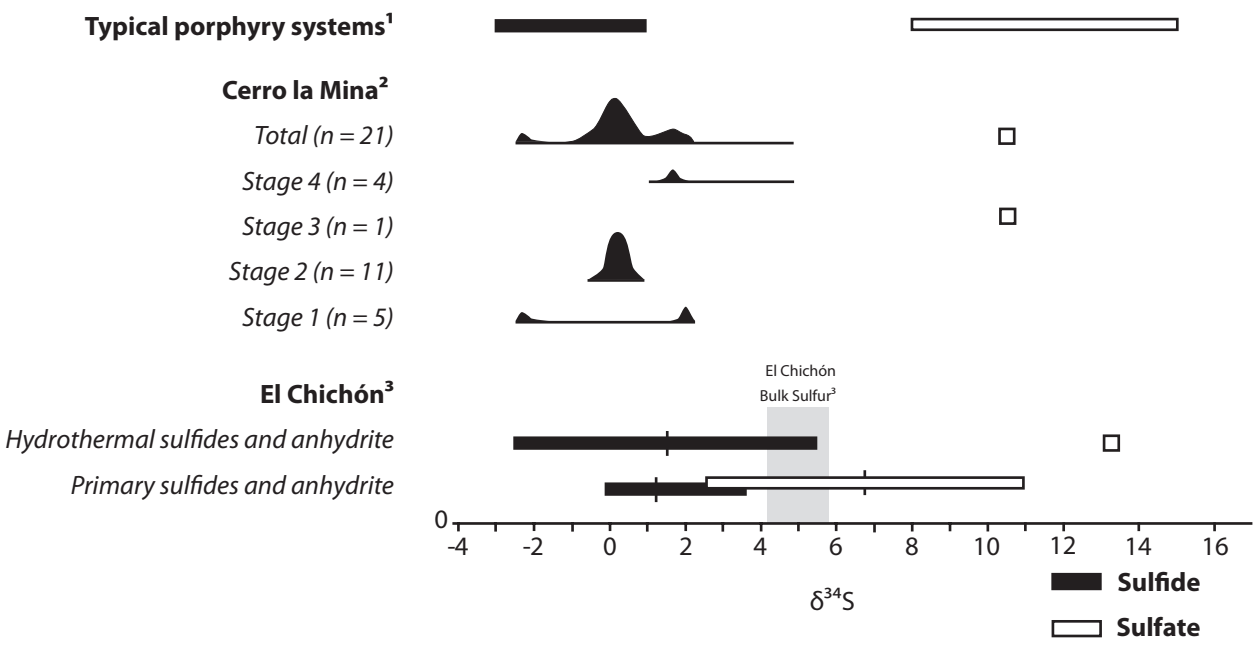

Fig. 14. Comparison of $\delta^{34}S$ values of El Chichón volcano and Cerro la Mina with typical porphyry systems. 1= Ohmoto and Rye, 1979; Ohmoto and Goldhaber, 1997; Wilson et al., 2007, 2 = This study, 3 = Rye et al., 1984; Luhr and Logan, 2002.

volcanic domes are associated with pyroclastic flow deposits, rare basalts, porphyritic hornblende andesites, trachyandesites, and minor rhyodacites and rhyolites (Damon and Motesinos, 1978; Duffield et al., 1984; Mora et al., 2007). The stratigraphy at Cerro la Mina is offset by a major NW-trending fault that has an orientation and movement consistent with the regional strike-slip structural regime, composed of a set of upthrown and downthrown blocks, bounded by left-lateral strike-slip faults in which it occurs (Fig. 1B; Meneses-Rocha, 2001; García-Palomo et al., 2004). The Cerro la Mina volcanic stratigraphy (Fig. 4) likely developed in a setting similar to that of the nearby El Chichón volcano, which has recorded a similar volcanic stratigraphy in a graben setting (García Palomo et al., 2004). The El Chichón volcanic record from 8,000 years ago to present consisted of tephra-falls, pyroclastic surges, pyroclastic flows, debris flows, and minor andesitic lava (Sigurdsson et al., 1984; Espindola et al., 2000).

The Cerro la Mina breccia pipe is a vertically oriented, cylindrical, and downward-tapering pipe. The core of pipe contains the fine-grained granular breccia (Unit 4A) and grades outward to coarser brecciated volcanic wall rocks (Unit 4B; Fig. 5J). The granule-sized central facies and outer zone of bimodal distribution of clastic material (i.e., clasts and matrix) are both indications that this rock formed by a fragmentation process that was efficient. Unit 4 was probably formed by a magmatic-hydrothermal fragmentation process, possibly explosive, and likely driven by volatile exsolution associated with a volatile-rich cooling intrusion/magma at depth (e.g., Burnham, 1981; Candela, 1991; Shinohara and Hedenquist, 1997).

The breccia pipe hosts the most significant alteration and mineralization textures that have been recognized to date at Cerro la Mina. Unit 4A has undergone pervasive advanced argillic-argillic alteration in many locations and can be difficult to recognize; much of Unit 4A's distribution on Figure 4B and E is interpreted. However, this unit can be readily identified on the margins of the pervasive advanced argillic-argillic alteration. The full extent of Unit 4 on the northeast side of the NW-trending fault is not known due to limited drilling and poor surface exposure (Fig. 4A).

Geochronology of the Cerro la Mina prospect

The Cerro la Mina hydrothermal system (Fig. 15) began with stage 1 pyrite associated with potassic alteration that is inferred to have a pre-breccia timing, with the formation of the breccia pipe removing the central portion of stage 1 pyrite; this caused an annular-shaped distribution (Fig. 10A) and fractured the coarse-grained pyrite into jigsaw-fit textures. This zonation is similar to the distribution of mineralization at El Teniente where the Braden breccia pipe has overprinted mineralization (Howell and Molloy, 1960), but in the case of Cerro la Mina, the breccia pipe has cut the distribution of stage 1 pyrite (Fig. 10A). The breccia pipe (Unit 4), likely formed by the eruption of hydrothermal fluids triggered by an intrusion at depth, cut the volcanic stratigraphy between the 1.04 ± 0.04 Ma (zircon U-Pb) intrusion of monzodiorites in the region (Unit 2; Jansen, 2012) and precipitation of stage 2 molybdenite at 780 ± 10 ka (Re-Os); this is consistent with the fact that the breccia pipe, which hosts the molybdenite, cuts the monzodiorite (Unit 2). The formation of the breccia pipe was followed by a second stage of abundant K-feldspar alteration.

Stage 2 mineralization and associated phyllic alteration occurred at 780 ± 10 ka (molybdenite Re-Os). The Re-Os age of molybdenite (780 ± 10 ka) is older than the $^{40}Ar/^{39}Ar$ biotite age (689 ± 13 ka), despite relative timing relationships showing that biotite formed first. The age discrepancy can be accounted for by the effects of closure temperatures,

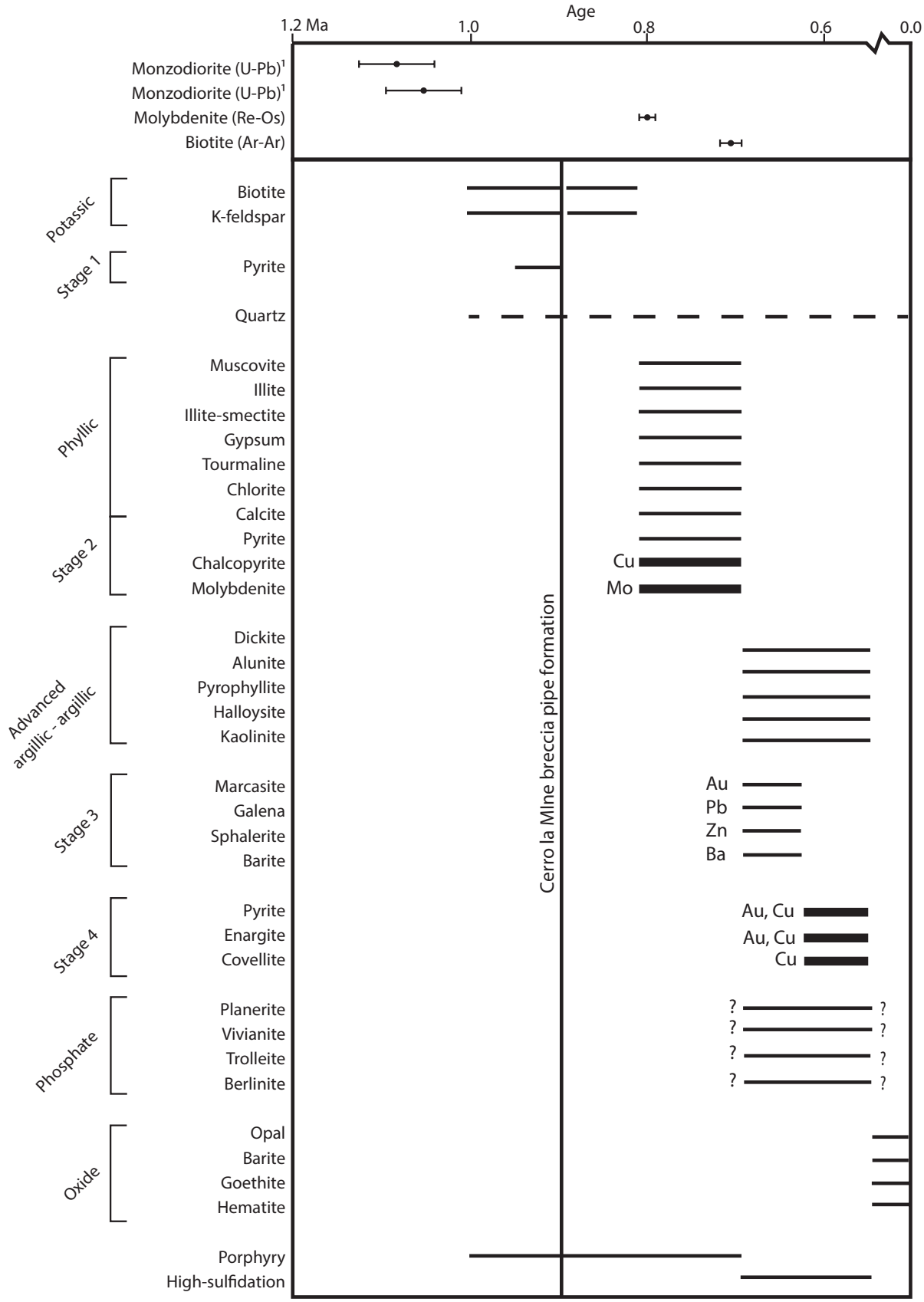

Fig. 15. Paragenesis of alteration and mineralization for the Cerro la Mina prospect and U-Pb, Re-Os, and $^{40}Ar/^{39}Ar$ ages for the Cerro la Mina prospect. Error bars are 2σ. [1] = Jansen (2012).

~500°C for molybdenite (Suzuki et al., 1996) and ~300°C for biotite (Harrison et al., 1985). The Re-Os age therefore represents the mineralization age of stage 2 and the biotite age records cooling of the system, specifically the transition from high-temperature phyllic to low-temperature advanced argillic-argillic alteration. From these data, an approximate cooling rate of 2°C/ka can be calculated. This cooling rate is exceptionally high when compared to a much larger and longer hydrothermal history such as the Chuquicamata porphyry deposit, which recorded a cooling rate of 0.1°C/ka (McInnes et al., 1999). The high cooling rate may be the result of a small intrusion, shallow intrusion depth, and/or efficient hydrothermal circulation (e.g., Cathles, 1977). The hydrothermal system terminated after 689 ± 13 ka (biotite Ar-Ar), approximately 300,000 years before El Chichón volcano began erupting.

Cerro la Mina stage 3–4 alteration

The initial hypogene acid leaching typically forms a core of residual quartz that grades outward to quartz-alunite, quartz-dickite-kaolinite and, finally, a propylitic assemblage in the wall rock (Steven and Ratte, 1960). A vertically extensive low-temperature (<110°C; Marumo and Hattori, 1999) alteration zone of halloysite + kaolinite extends deeper than the dickite ± alunite ± pyrophyllite zone (Fig. 7B, E). The buffering effect of the host alkaline volcanic rocks may have prevented the production of strongly acidic fluids, resulting in the production of abundant argillic clays rather than residual quartz.

The Cerro la Mina alteration assemblage of quartz + dickite ± kaolinite ± pyrophyllite ± alunite, typically occurs at 120° to 260°C in active geothermal systems (e.g., Reyes, 1990). The deep occurrence of the Cerro la Mina halloysite alteration may indicate a higher temperature of formation than typically expected of <110°C (Marumo and Hattori, 1999; Joussein et al., 2005), or alternately, a relatively deep occurrence of low-temperature alteration in the latest stage.

A minimum temperature of halloysite formation is suggested by the association with marcasite and pyrite, which form at temperatures greater than 40°C (Reyes, 1990; Hedenquist et al., 2000). We therefore consider the most reasonable temperature of formation for the Cerro la Mina halloysite, consistent with mineral associations and other studies (e.g., Marumo and Hattori, 1999), to be 40° to 120°C. The low formation temperature for Cerro la Mina halloysite is within the range of supergene (<~60°C; Melchiorre et al., 2000) and steam-heated conditions (90° to 160°C; Rye et al., 1992) rather than hypogene acidic alteration, which typically ranges between 160° to 260°C (Hedenquist and Taran, 2013). The vertical distribution, rather than a horizontal distribution of a paleogroundwater table, argues against the possibility of a steam-heated or supergene origin for the halloysite alteration (e.g., Hedenquist et al., 2000). In addition, the association of halloysite with sulfides (Kyne et al., 2013) that have ^{34}S values consistent with a magmatic source supports a hypogene origin.

Sulfur isotopes

The sulfur isotope composition of Cerro la Mina sulfides (Fig. 14; range, –2.5 to +4.9‰; mean 0.7‰) and sulfates (Fig. 14; +10.5‰) were investigated to test whether a component of sulfur was derived from a thick (>770 m) sequence of ^{34}S-enriched Lower Cretaceous evaporites ($\delta^{34}S$ = +15.1‰; Rye et al., 1984) and/or the host volcanic rocks. The Cerro la Mina $\delta^{34}S$ sulfide values are lower than the average total $\delta^{34}S$ (sulfide and sulfate) for andesites in island-arc environments (+5 to +7‰; Ueda and Sakai, 1984; Woodhead et al., 1987) and El Chichón estimated bulk magma $\delta^{34}S$ value of +4.1 to +5.8‰ (Rye et al., 1984; Luhr and Logan, 2002) suggesting the fluid was slightly oxidized. A shift to higher $\delta^{34}S$ sulfide and sulfate values, as would be expected if significant incorporation of $\delta^{34}S$ in the hydrothermal fluid from the Cretaceous evaporites, was not observed. Likewise, there is no shift toward heavier $\delta^{34}S$ values to suggest involvement of sulfur accumulated by circulating meteoric water through the Selva Negra volcanic host rocks. The hydrothermal fluid responsible for the deposition of sulfides and sulfates at Cerro la Mina was most likely a fluid dominated by magmatic components.

El Chichón high-sulfur and high $\delta^{34}S$ magmatism has been suggested by some to be the result of prior loss of ^{34}S-depleted H_2S to a fluid or gas phase during formation of a small, porphyry-type hydrothermal system or ore deposit (Luhr, 1983; Rye et al., 1984; Luhr and Logan, 2002; Rye, 2005) as the incorporation of thick ^{34}S-enriched Lower Cretaceous evaporites has been discounted (Rye et al., 1984; Luhr and Logan, 2002). The range of $\delta^{34}S$ sulfides and sulfates obtained from the Cerro la Mina prospect is similar to that in the lithic fragments of porphyry mineralization that erupted from El Chichón (Fig. 14). The El Chichón lithic fragments of porphyry copper-type mineralization have 1-mm-wide anhydrite veinlets with K-feldspar and biotite alteration and disseminated Cu-rich pyrrhotite (Luhr, 1983; Rye et al., 1984). Both the sulfide and sulfate $\delta^{34}S$ values for Cerro la Mina and El Chichón volcano also overlap with the range of porphyry deposits worldwide (Fig. 14; Ohmoto and Rye, 1979; Ohmoto and Goldhaber, 1997; Wilson et al., 2007). The single $\delta^{34}S$ value for barite at Cerro la Mina overlaps with the range of primary anhydrite and is lighter than the single $\delta^{34}S$ value of hydrothermal anhydrite from El Chichón.

Cerro la Mina and El Chichón alkaline affinities

The alkaline composition of young volcanic rocks in the region (García Palomo et al., 2004; Jansen, 2012) suggests that a buried intrusive stock may have the same composition. Alkalic porphyry deposits are well-documented from British Columbia (e.g., Hollister, 1978; Schroeter, 1995; Lang et al., 1995; Bath et al., 2014; Byrne and Tosdal, 2014; Jago et al., 2014; Micko et al., 2014; Pass et al., 2014) and eastern Australia (Heithersay and Walshe, 1995; Lickfold et al., 2003; Wilson et al., 2003; Cooke et al., 2007; Wilson et al., 2007; Zukowski, 2010), but few examples have been described in the eastern alkaline province of northeastern Mexico (Mutschler et al., 1998; Hammarstrom et al., 2010) or from other terrains (e.g., Jensen and Barton, 2000; Carman, 2003; Wolfe and Cooke, 2011). There are occurrences of alkalic rocks that are associated with large gold deposits because of their hydrous and oxidized nature and their ability to produce hydrothermal systems with ideal chemistries for transporting gold (Richards, 1995). Alkalic Au-(Cu)

porphyry deposits include some of the world's highest-grade porphyry gold resources (e.g, Ridgeway; Wilson et al., 2003) and some of the largest gold accumulations in epithermal environments (e.g., Cripple Creek and Lihir; Jensen and Barton, 2000; Mungall, 2002; Blackwell et al., 2014).

The early K-feldspar and biotite at Cerro la Mina are similar to what is found Ladolam, Lihir Island, where early biotite–K-feldspar alteration predated the alkalic epithermal mineralization (Carman, 1994; Müller et al., 2002). Early biotite alteration has also been recognized as a precursor to alkali-related epithermal mineralization at Cripple Creek and Porgera (Ronacher et al., 2004). The El Chichón lithic fragments contain anhydrite veining and alteration which can occur in both calc-alkalic and alkalic porphyry deposits, e.g., Galore Creek (Byrne and Tosdal, 2014; Micko et al., 2014), Mt. Polley (Pass et al., 2014), Ampucao (Cooke et al., 2011), and El Teniente (Cannell et al., 2005).

Metallogeny of the Chiapanecan volcanic arc

The Santa Fé mine, Cerro la Mina prospect, and Campamento deposit likely represent proximal skarn, porphyry/high-sulfidation, and intermediate sulfidation components, respectively, according to the porphyry model of Sillitoe (2010). These mineralization occurrences may be related, and they indicate a district-wide zoning pattern that may suggest other targets in the district and elsewhere in the Chiapanecan volcanic arc.

The Santa Fé skarn deposit can be considered representative of mineralization encountered in the deeper parts of the district where granodiorite to diorite intrusions are in contact with either Paleogene or Cretaceous limestone (Fig. 3A). Therefore, exploration for Santa Fé style mineralization should be conducted where erosional levels are deepest and closer to this intrusion-limestone contact to increase chances of discovery, particularly in the Santa Fé region (Fig. 3A) and to the north and west of Cerro la Mina (Fig. 3B). The Campamento Au-Ag and Cerro la Mina prospects present mineralization that occurs at shallow levels of erosion where Pliocene to Pleistocene volcanic rocks are preserved. The district alteration is centered on the Cerro la Mina prospect (Fig. 6A), which occurs along a major through-going structure. In this scenario, the Campamento Au-Ag epithermal deposit may be a distal feature. The systematic changes in the spectral features of the white mica assemblage can be used as an exploration vector because the shift to lower wavelength position of the Al-OH spectral absorption feature and high crystallinity may suggest the potential for epithermal mineralization similar to Cerro la Mina (Fig. 6B).

The characteristics of Cerro la Mina and Campamento are a variation of the conventional epithermal deposits (e.g., Seedorff et al., 2005; Sillitoe, 2010) and broaden the window for additional discoveries in this setting. Cerro la Mina has extensive low-temperature hypogene halloysite + kaolinite, rare alunite. The nearby Campamento deposit, which occurs on the margin of the extensive alteration of the Cerro la Mina prospect, contains abundant high-grade narrow carbonate ± clay ± rare quartz alteration assemblages (Jansen, 2007). Campamento fluid inclusion studies suggest a similarity to alkali-related epithermal gold deposits (e.g., Cripple Creek: Thompson, 1996, and Lihir: Ageneau, 2013).

Conclusion: Genesis of the Cerro la Mina Prospect

The Cerro la Mina prospect is hosted by Pleistocene alkaline volcanic rocks of the Selva Negra that formed in a complex triple-junction tectonic setting. The stratigraphy (Fig. 4) suggests that volcanism occurred in a setting analogous to that of the nearby El Chichón volcano (García Palomo et al., 2004), with large volumes of pyroclastic and volcanic debris flows deposited in a graben setting (Fig. 16A). The region has been and continues to be under a regional left-lateral strike-slip structural regime (Fig. 1B; Meneses-Rocha, 2001; García-Palomo et al., 2004) that includes a NW-trending sinistral wrench fault that was active throughout the history of Cerro la Mina and is responsible for dismembering the prospect after mineralization (Figs. 4A, 16).

Potassic-altered rocks and stage 1 pyrite (Fig. 16B) were cut by the breccia pipe (Fig. 16C), between 1.04 ± 0.04 (U-Pb zircon) and 780 ± 10 ka (Re-Os molybdenite; Fig. 16C). The development of the breccia pipe provided a permeable host for subsequent alteration and mineralization. The ensuing hydrothermal system consisted of four mineralization stages associated with three alteration assemblages. A weakly developed porphyry system at 780 ± 10 ka (Re-Os date on molybdenite) introduced Cu and Mo (stage 2 pyrite ± chalcopyrite ± molybdenite ± quartz veins; Fig. 16D) along with phyllic alteration. The phyllic alteration produced a large thermal footprint extending up to 2 km from the breccia pipe (Fig. 6A). In addition, the crystallinity and Al-OH peak shifts in spectral data (Fig. 6B) suggest that the major heat center for the district is centered on the breccia pipe and at depth. The hydrothermal system cooled below the closure temperature of biotite (~300°; Harrison et al., 1985) at <689 ± 13 ka and evolved into a high sulfidation epithermal system (arsenian pyrite + enargite) that introduced the highest grades of Au and Cu (stage 3 marcasite, sphalerite, galena, and barite, and stage 4 arsenian pyrite ± enargite ± covellite; Fig. 16E). The high sulfidation system produced an extensive alteration of halloysite + kaolinite that occurred deeper and at a lower temperature (<120°C) than the high-temperature alteration assemblage of quartz + dickite ± kaolinite ± pyrophyllite ± alunite; Fig. 7B, E). A northwest fault offset a portion of the system (Fig. 7A, E).

The positive $\delta^{34}S$ sulfide values for Cerro la Mina mineralization (Fig. 14) are consistent with mineral deposition from a reduced (sulfide dominant), high-temperature (>400°C) magmatic-hydrothermal fluid (Ohmoto and Rye, 1979; Rye, 1993). The apparent lack of strongly acidic fluids required to produce residual quartz and extensive alunite may have been related to the buffering capacity of the alkaline host rocks.

The Santa Fé mine, Cerro la Mina prospect, and Campamento deposit are representative of parts of a porphyry copper system, specifically a proximal skarn, porphyry/high-sulfidation, and intermediate sulfidation deposits, respectively (Fig. 16F). The characteristics of Cerro la Mina (i.e, anomalous halloysite-kaolinite alteration) broaden the window for additional discoveries in the porphyry-epithermal environment. The alkaline composition of volcanic rocks suggests that Cerro la Mina may have potential for gold mineralization at greater depths in the breccia pipe, or in the poorly explored

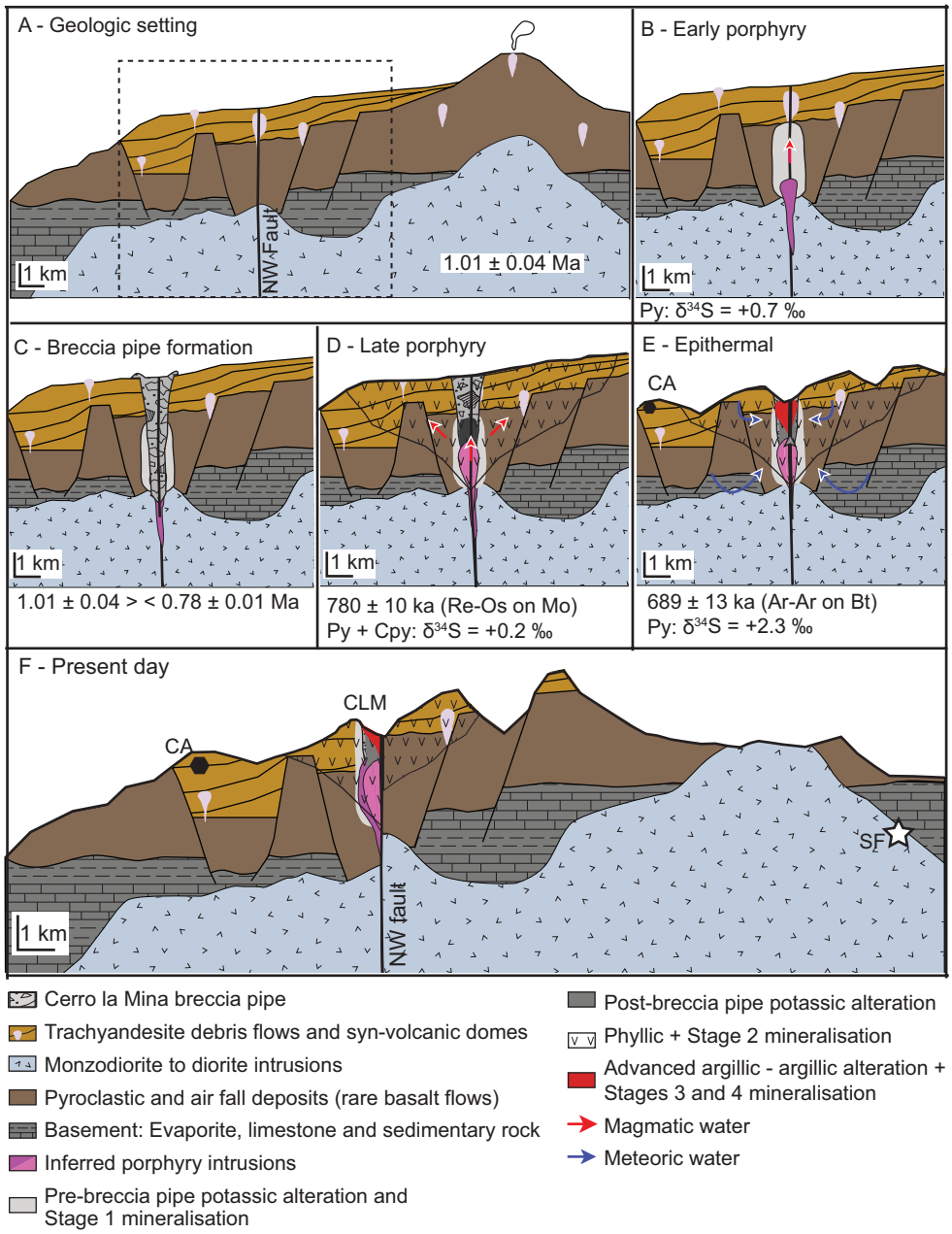

Fig. 16. Schematic presentation of the geologic setting and formation of the Cerro la Mina Au (Cu-Mo) prospect. Figure described in text. Abbreviations: Bt = biotite, CA = Campamento Au-Ag deposit, Cpy = chalcopyrite, Mo = molybdenite, Py = pyrite, SF = Santa Fé skarn deposit.

northeast section of the prospect where the offset part of the deposit is yet to be discovered.

Acknowledgments

This study was initiated as part of AMIRA International project P765A, Geochemical Halos in Green Rocks and Lithocaps: The Explorers' Toolbox for Porphyry and Epithermal Districts, at the ARC Centre of Excellence for Ore Deposit Research (CODES) at the University of Tasmania. We thank our sponsors, AngloGold Ashanti, Anglo American, Barrick, Buenaventura, Codelco, Dundee, Equinox, Freeport-McMoran, Gold Fields, Kinross, MMG, Newcrest, Newmont, St. Barbara Rio Tinto, Teck, Vale, and Xstrata for their technical support. We gratefully acknowledge Kinross and Fortune Bay for providing field support and access to the Cerro la Mina prospect. Additional financial support was provided by a Natural Science and Engineering Research Council collaborative research development grant to Hollings. We would like to thank the Society of Economic Geologists for the Graduate Student Research Fellowship Award and the University of Tasmania for the Endeavour International Postgraduate Research Scholarship. We thank Jacqueline Blackwell, Jeffrey Hedenquist, and Peter Megaw for their useful reviews.

REFERENCES

Ageneau, M., 2013, Geology of the Kapit ore zone and comparative geochemistry with Minifie and Lienetz ore zones, Ladolam gold deposit, Lihir Island, Papua New Guinea: Unpublished PhD thesis, University of Tasmania, Australia, 297 p.

Bailey, E.M., and Stevens, R.E., 1960, Selective staining of K-feldspar and plagioclase on rock slabs and thin sections: American Mineralogist, v. 45, p. 1020–1025.

Barton, M.D., Staude, J.M., Zürcher, L., and MeGaw, P.K.M., 1995, Porphyry copper and other intrusion-related mineralization in Mexico, *in* Pierce, F.W., and Bolm, J.G., eds., Porphyry copper deposits of the American Cordillera: Arizona Geological Society Digest, v. 20, p. 487–524.

Bath, A.B., Cooke, D.R., Friedman, R.M., Faure, K., Kamenetsky, V.S., Tosdal, R.M., and Berry, R.F., 2014, Mineralization, U-Pb geochronology, and stable isotope geochemistry of the lower main zone of the Lorraine deposit, north-central British Columbia: A replacement-style alkalic Cu-Au porphyry: Economic Geology, v. 109, p. 979–1004.

Blackwell, J.L., Cooke, D.R., McPhie, J., and Simpson, K.A., 2014, Lithofacies associations and evolution of the volcanic host succession to the Minifie ore zone: Ladolam gold deposit, Lihir Island, Papua New Guinea: Economic Geology, v. 109, p. 1137–1160.

Burbach, G.V., Frohlich, C., Pennington, W.D., and Matumoto, T., 1984, Seismicity and tectonics of the subducted Cocos plate: Journal of Geophysical Research, v. 89, p. 7719–7735.

Burnham, C.W., 1981, Physicochemical constraints on porphyry mineralization: Geological Society of Arizona Digest, v. 14, p. 71–77.

Byrne, K., and Tosdal, R.M., 2014, Genesis of the Late Triassic southwest zone breccia-hosted alkalic porphyry Cu-Au deposit, Galore Creek, British Columbia, Canada: Economic Geology, v. 109, p. 915–938.

Camprubí, A., and Albinson, T., 2007, Epithermal deposits in Mexico—update of current knowledge, and an empirical reclassification: Geological Society of America Special Papers, v. 422, p. 377–415.

Candela, P.A., 1991, Physics of aqueous phase evolution in plutonic environments: American Mineralogist, v. 76, p. 1081–1091.

Cannell, J., Cooke, D.R., Walshe, J.L., and Stein, H., 2005, Geology, mineralization, alteration, and structural evolution of the El Teniente porphyry Cu-Mo deposit: Economic Geology, v. 100, p. 979–1003.

Carman, G.D., 1994, Genesis of the Ladolam gold deposit, Lihir Island, Papua New Guinea: Unpublished PhD thesis, Victoria, Australia, Monash University, 300 p.

——2003, Geology, mineralization and hydrothermal evolution of the Ladolam gold deposit, Lihir Island, Papua New Guinea: Society of Economic Geologists, Special Publication no. 10, p. 247–284.

Carroll, M.R., and Rutherford, M.J., 1987, The stability of igneous anhydrite: Experimental results and implications for sulfur behavior in the 1982 El Chichon trachyandesite and other evolved magmas: Journal of Petrology, v. 28, p. 781–801.

Cathles, L.M., 1977, An analysis of the cooling of intrusives by ground-water convection which includes boiling: Economic Geology, v. 72, p. 804–826.

Chang, Z., Hedenquist, J.W., White, N.C., Cooke, D.R., Roach, M., Deyell, C.L., Garcia, J., Gemmell, J.B., McKnight, S., and Cuison, A.L., 2011, Exploration tools for linked porphyry and epithermal deposits: Example from the Mankayan intrusion-centered Cu-Au district, Luzon, Philippines: Economic Geology, v. 106, p. 1365–1398.

Cooke, D.R., Wilson, A.J., House, M.J., Wolfe, R.C., Walshe, J.L., Lickfold, V., and Crawford, A.J., 2007, Alkalic porphyry Au -Cu and associated mineral deposits of the Ordovician to Early Silurian Macquarie Arc, New South Wales: Australian Journal of Earth Sciences, v. 54, p. 445–463.

Cooke, D.R., Deyell, C.L., Waters, P.J., Gonzales, R.I., and Zaw, K., 2011, Evidence for magmatic-hydrothermal fluids and ore-forming processes in epithermal and porphyry deposits of the Baguio district, Philippines: Economic Geology, v. 106, p. 1399–1424.

Damon, P.E., and Motesinos, E., 1978, Late Cenozoic volcanism and metallogenesis over an active Benioff zone in Chiapas, Mexico: Arizona Geological Society Digest, v. 11, p. 155–168.

Damon, P.E., Shafiqullah, M., and Clark, K.F., 1983, Geochronology of the porphyry copper deposits and related mineralization of Mexico, *in* Dawson, K.M., ed., Symposium; Metallogeny and tectonics of the North American Cordillera: Canadian Journal of Earth Sciences, v. 20, p. 1052–1071.

Duffield, W.A., Tilling, R.I., and Canul, R., 1984, Geology of El Chichon Volcano, Chiapas, Mexico: Journal of Volcanology and Geothermal Research, v. 20, p. 117–132.

Escandón Valle, F.J., Gómez de la Rosa, E., Salinas Prieto, J.C., De la Calleja Moctezuma, A., Sánchez Rojas, L.E., Barajas Nigoche, L.D., and Salinas Prieto, J.C., 2006, Carta geológico Mexicano estados de Chiapas y Tabasco, Servicio Geológico Mexicano, scale 1:500,000.

Espindola, J.M., Macias, J.L., Tilling, R.I., and Sheridan, M.F., 2000, Volcanic history of El Chichón Volcano (Chiapas, Mexico) during the Holocene, and its impact on human activity: Bulletin of Volcanology, v. 62, p. 90–104.

García-Palomo, A., Macías, J.L., and Espíndola, J.M., 2004, Strike-slip faults and K-alkaline volcanism at El Chichón volcano, southeastern Mexico: Journal of Volcanology and Geothermal Research, v. 136, p. 247–268.

García-Palomo, A., Macías, J.L., Arce, J.L., Mora, J.C., Saucedo, R., Espíndola, J.M., Escobar, R., and Layer, P., 2006, Geological evolution of the Tacaná Volcanic Complex, México-Guatemala, Special Paper of the Geological Society of America, p. 39–57.

Guzman-Speziale, M., and Meneses-Rocha, J.J., 2000, The North America-Caribbean plate boundary west of the Motagua-Polochic fault system: A fault jog in southeastern Mexico: Journal of South American Earth Sciences, v. 13, p. 459–468.

Hammarstrom, J.M., Robinson, G.R., Jr., Ludington, S., Gray, F., Drenth, B.J., Cendejas-Cruz, F., Espinosa, E., Pérez-Segura, E., Valencia-Moreno, M., Rodríguez-Castañeda, J.L., Vásquez-Mendoza, R., and Zürcher, L., 2010, Global mineral resource assessment—porphyry copper assessment of Mexico: U.S. Geological Survey Scientific Investigations Report 2010–5090-A, 176 p.

Harrison, T.M., Duncan, I., and McDougall, I., 1985, Diffusion of ^{40}Ar in biotite: Temperature, pressure and compositional effects: Geochimica et Cosmochimica Acta, v. 49, p. 2461–2468.

Hedenquist, J.W., and Taran, Y.A., 2013, Modeling the formation of advanced argillic lithocaps: Volcanic vapor condensation above porphyry intrusions: Economic Geology, v. 108, p. 1523–1540.

Hedenquist, J.W., Arribas, A.R., and Gonzalez-Urien, E., 2000, Exploration for epithermal gold deposits: Reviews in Economic Geology, v. 13, p. 245–277.

Heithersay, P.S., and Walshe, J.L., 1995, Endeavour 26 North: A porphyry copper-gold deposit in the late Ordovician, Shoshonitic Goonumbla Volcanic Complex, New South Wales, Australia: Economic Geology, v. 90, p. 1506–1532.

Hollister, V.F., 1978, Geology of the porphyry copper deposits of the Western Hemisphere: New York, Society of Mining Engineers of the American Institute of Mining, Metallurgical, and Petroleum Engineers, 219 p.

Howell, F.H., and Molloy, J.S., 1960, Geology of the Braden orebody, Chile, South America: Economic Geology, v. 55, p. 863–905.

Huston, D.L., Power, M., Gemmell, J.B., and Large, R., 1995, Design, calibration and geologic application of the first operational Australian laser ablation sulphur isotope microprobe: Australian Journal of Earth Sciences, v. 42, p. 549–555.

Jago, C.P., Tosdal, R.M., Cooke, D.R., and Harris, A.C., 2014, Vertical and lateral variation of mineralogy and chemistry in the Early Jurassic Mt. Milligan alkalic porphyry Au-Cu deposit, British Columbia, Canada: Economic Geology, v. 109, p. 1005–1033.

Jansen, N.H., 2007, An infrared spectral reflectance study of the hydrothermal alteration minerals from the Campamento Au/Ag deposit, southern Mexico: Unpublished honours thesis, Nova Scotia, Canada, Saint Mary's University, 92 p.

——2012, Geology and genesis of the Cerro la Mina porphyry-high sulfidation prospect, Mexico: Unpublished PhD thesis, Australia, University of Tasmania, 222 p.

Jensen, E.P., and Barton, M.D., 2000, Gold deposits related to alkaline magmatism, Reviews in Economic Geology, v. 13, p. 279–314.

Jourdan, F., Féraud, G., Bertrand, H., Watkeys, M.K., and Renne, P.R., 2007, Distinct brief major events in the Karoo large igneous province clarified by new $^{40}Ar/^{39}Ar$ ages on the Lesotho basalts: Lithos, v. 98, p. 195–209.

Joussein, E., Petit, S., Churchman, J., Theng, B., Righi, D., and Delvaux, B., 2005, Halloysite clay minerals - a review: Clay Minerals, v. 40, p. 383–426.

Krueger, A.J., Walter, L.S., Bhartia, P.K., Schnetzler, C.C., Krotkov, N.A., Sprod, I., and Bluth, G.J.S., 1995, Volcanic sulfur dioxide measurements from the total ozone mapping spectrometer instruments: Journal of Geophysical Research: Atmospheres, v. 100, p. 14,057–14,076.

Kyne, R., Hollings, P., Jansen, N.H., and Cooke, D., 2013, Supergene and hypogene halloysite in a porphyry-epithermal environment at Cerro la Mina, Chiapas, Mexico: Economic Geology, v. 108, p. 1147–1161.

Lang, J.R., Lueck, B., Mortensen, J.K., Kelly Russell, J., Stanley, C.R., and Thompson, J.F.H., 1995a, Triassic-Jurassic silica-undersaturated and

silica-saturated alkalic intrusions in the Cordillera of British Columbia: Implications for arc magmatism: Geology, v. 23, p. 451–454.
Layer, P.W., Garcia-Polomo, A., Jones, D., Macias, J.L., Arce, J.L., and Mora, J.C., 2009, El Chichón volcanic complex, Chiapas, México: Stages of evolution based on field mapping and $^{40}Ar/^{39}Ar$ geochronology: Geofisica Internacional, v. 48, p. 33–54.
Lee, J.-Y., Marti, K., Severinghaus, J.P., Kawamura, K., Yoo, H.-S., Lee, J.B., and Kim, J.S., 2006, A redetermination of the isotopic abundances of atmospheric Ar: Geochimica et Cosmochimica Acta, v. 70, p. 4507–4512.
Lickfold, V., Cooke, D.R., Smith, S.G., and Ullrich, T.D., 2003, Endeavour copper-gold porphyry deposits, Northparkes, New South Wales: Intrusive history and fluid evolution: Economic Geology, v. 98, p. 1607–1636.
Linear Gold Corp., 2007, Linear Gold Corporation website, Linear Gold Corporation, p. http://lineargoldcorp.com.
Luhr, J.F., 1983, The 1982 eruptions of El Chichon and the relationship to mineralized magmatic-hydrothermal systems [abs.]: Geological Society of America, Abstracts with Programs, v. 15, p. 632.
——2008, Primary igneous anhydrite: Progress since its recognition in the 1982 El Chichón trachyandesite: Journal of Volcanology and Geothermal Research, v. 175, p. 394–407.
Luhr, J.F., and Logan, M.A.V., 2002, Sulfur isotope systematics of the 1982 El Chichon trachyandesite: An ion microprobe study: Geochimica et Cosmochimica Acta, v. 66, p. 3303–3316.
Luhr, J.F., Carmichael, I.S.E., and Varekamp, J.C., 1984, The 1982 eruptions of El Chichon volcano, Chiapas, Mexico: Mineralogy and petrology of the anhydrite bearing pumices: Journal of Volcanology and Geothermal Research, v. 23, p. 69–108.
MacCarthy, E.T., 1897, Mining in the wollastonite ore-deposits of the Santa Fé mine, Chiapas: Transactions of the Institution of Mining and Metallurgy, v. 4, p. 169–189.
Mandujano-Velazquez, J.J., and Keppie, J.D., 2009, Middle Miocene Chiapas fold and thrust belt of Mexico: A result of collision of the Tehuantepec transform/ridge with the Middle America trench, Geological Society Special Publication, p. 55–69.
Martinez Lopez, F., 2009, Ixhuatán geologic map: Toronto, Kinross Gold Corporation, scale 1:10,000..
Marumo, K., and Hattori, K.H., 1999, Seafloor hydrothermal clay alteration at Jade in the back-arc Okinawa Trough: Mineralogy, geochemistry and isotope characteristics: Geochimica et Cosmochimica Acta, v. 63, p. 2785–2804.
McInnes, B.I.A., Farley, K.A., Sillitoe, R.H., and Kohn, B.P., 1999, Application of apatite (U-Th)/He thermochronometry to the determination of the sense and amount of vertical fault displacement at the Chuquicamata porphyry copper deposit, Chile: Economic Geology, v. 94, p. 937–947.
McPhie, J., Doyle, M., and Allen, R.L., 1993, Volcanic textures: A guide to the interpretation of textures in volcanic rocks: University of Tasmania, Centre for Ore Deposit and Exploration Studies, 196 p.
Medina, F., Gonzalez-Moran, T., and Gonzalez, L., 1990, Gravity and seismicity analyses of the El Chichon volcano, Chiapas, Mexico: Pageoph, v. 133, p. 149–165.
Melchiorre, E.B., Criss, R.E., and Rose, T.P., 2000, Oxygen and carbon isotope study of natural and synthetic azurite: Economic Geology, v. 95, p. 621–628.
Meneses-Rocha, J.J., 2001, Tectonic evolution of the Ixtapa Graben, an example of a strike-slip basin of southeastern Mexico: Implications for regional petroleum systems: American Association of Petroleum Geologists Memoir, v. 75, p. 183–216.
Micko, J., Tosdal, R.M., Bissig, T., Chamberlain, C.M., and Simpson, K.A., 2014, Hydrothermal alteration and mineralization of the Galore Creek alkalic Cu-Au porphyry deposit, northwestern British Columbia, Canada: Economic Geology, v. 109, p. 891–914.
Miranda-Gasca, M.A., Pyle, P., Roldán, J., Ochoa-Camarillo, H.R., Arias, R., and Jaimez, A., 2009, Los depósitos de oro-plata y cobre-oro en Ixhuatán y Santa Fé, Chiapas, México, *in* Clark, F.C., Salas-Pizá, G.A., and Cubillas-Estrada, R., ed., Geología Económica de México: Asociación de Ingenieros de Minas, Metalurgistas y Geólogos de Mexico, 2nd edition, A.C., Servicio Geologico Mexicano, p. 379–381.
Mora, J.C., Jaimes-Viera, M.C., Garduno-Monroy, V.H., Layer, P.W., Pompa-Mera, V., and Gondinez, M.L., 2007, Geology and geochemistry characteristics of the Chiapanecan volcanic arc (Central Area), Chiapas Mexico: Journal of Volcanology and Geothermal Research, v. 162, p. 43–72.
Müller, D., Kaminski, K., Uhlig, S., Graupner, T., Herzig, P., and Hunt, S., 2002, The transition from porphyry- to epithermal-style gold mineralization at Ladolam, Lihir Island, Papua New Guinea: A reconnaissance study: Mineralium Deposita, v. 37, p. 61–74.
Mungall, J.E., 2002, Roasting the mantle: Slab melting and the genesis of major Au and Au-rich Cu deposits: Geology, v. 30, p. 915–918.
Mutschler, F.E., McLemore, V.T., Bookstrom, A.A., and Ludington, S., 1998, Rocky Mountain Front alkalic rock-related gold deposits, Canada to Mexico, a review [abs.]: Geological Society of America Abstracts with Programs, 30, p. 300.
Nixon, G.T., 1982, The relationship between Quaternary volcanism in central Mexico and the seismicity and structure of subducted ocean lithosphere: Geological Society of America Bulletin, v. 93, p. 514–523.
Ohmoto, H., and Goldhaber, M.B., 1997, Sulfur and carbon isotopes, *in* Barnes, H.L., ed., Geochemistry of hydrothermal ore deposits: New York, John Wiley and Sons, p. 517–600.
Ohmoto, H., and Rye, R.O., 1979, Isotopes of sulfur and carbon, *in* Barnes, H.L., ed., Geochemistry of hydrothermal ore deposits: New York, Wiley Interscience, p. 509–567.
Pantoja, A., 1991, The Santa Fé mine, Chiapas, *in* Salas, G.P., ed., The geology of North America: Geological Society of America, v. P-3, Economic Geology, Mexico,p. 327–328.
Pass, H.E., Cooke, D.R., Davidson, G., Maas, R., Dipple, G., Rees, C., Ferreira, L., Taylor, C., and Deyell, C.L., 2014, Isotope geochemistry of the Northeast zone, Mount Polley alkalic Cu-Au-Ag porphyry deposit, British Columbia: A case for carbonate assimilation: Economic Geology, v. 109, p. 859–890.
Reyes, A.G., 1990, Petrology of Philippine geothermal systems and the application of alteration mineralogy to their assessment: Journal of Volcanology and Geothermal Research, v. 43, p. 279–309.
Richards, J.P., 1995, Alkalic-type epithermal gold deposits—a review, *in* Thompson, J.F.H., ed., Magmas, fluids, and ore deposits: Mineralogical Association of Canada, Short Course Series, v. 23, p. 367–400.
Robin, C., 1982, Mexico, *in* Thorpe, R.S., ed., Andesites: Orogenic andesites and related rocks: Chichester, John Wiley, p. 137–147.
Robinson, B.W., and Kusakabe, M., 1975, Quantitative preparation of sulfur dioxide, for $^{34}S/^{32}S$ analyses, from sulfides by combustion with cuprous oxide: Analytical Chemistry, v. 47, p. 1179–1181.
Ronacher, E., Richards, J.P., Reed, M.H., Bray, C.J., Spooner, E.T.C., and Adams, P.D., 2004, Characteristics and evolution of the hydrothermal fluid in the north zone high-grade area, Porgera gold deposit, Papua New Guinea: Economic Geology, v. 99, p. 843–867.
Rose, W.I., Bornhorst, T.J., Halsor, S.P., Capaul, W.A., Plumley, P.S., Dela Cruz-Reyna, S., Mena, M., and Mota, R., 1984, Volcán El Chichón, Mexico: Pre-1982 S-rich eruptive activity: Journal of Volcanology and Geothermal Research, v. 23, p. 147–149, 155–167.
Rye, R.O., 1993, The evolution of magmatic fluids in the epithermal environment: The stable isotope perspective: Economic Geology, v. 88, p. 733–752.
——2005, A review of the stable-isotope geochemistry of sulfate minerals in selected igneous environments and related hydrothermal systems: Chemical Geology, v. 215, p. 5–36.
Rye, R.O., Luhr, J.F., and Wasserman, M.D., 1984, Sulfur and oxygen isotopic systematics of the 1982 eruptions of El Chichon Volcano, Chiapas, Mexico: Journal of Volcanology and Geothermal Research, v. 23, p. 109–123.
Rye, R.O., Bethke, P.M., and Wasserman, M.D., 1992, The stable isotope geochemistry of acid sulfate alteration: Economic Geology, v. 87, p. 225–262.
Sánchez-Montes De Oca, R., 1979, Geología petrolera de la Sierra de Chiapas: Boletín de la Asociación Mexicana de Geólogos Petroleros, v. 31, p. 67–97.
Sasaki, A., and Ishihara, S., 1979, Sulfur isotopic composition of the magnetite-series and ilmenite-series granitoids in Japan: Contributions to Mineralogy and Petrology, v. 68, p. 107–115.
Schroeter, T.G., 1995, Porphyry deposits of the northwestern Cordillera of North America: Canadian Institute of Mining, Metallurgy and Petroleum, 46, p. 888.
Seedorff, E., Dilles, J.H., Proffett, J.M., Jr., Einaudi, M.T., Zurcher, L., Stavast, W.J.A., Johnson, D.A., and Barton, M.D., 2005, Porphyry deposits: Characteristics and origin of hypogene features: Economic Geology 100th Anniversary Volume, p. 251–298.
Shinohara, H., and Hedenquist, J.W., 1997, Constraints on magma degassing beneath the Far Southeast porphyry Cu-Au deposit, Philippines: Journal of Petrology, v. 38, p. 1741–1752.
Sigurdsson, H., Carey, S.N., and Espíndola, J.M., 1984, The 1982 eruptions of El Chichón Volcano, Mexico: Stratigraphy of pyroclastic deposits: Journal of Volcanology and Geothermal Research, v. 23, p. 11–37.

Sillitoe, R.H., 1976, Reconnaissance of the Mexican porphyry copper belt: Transactions of the Institution of Mining and Metallurgy, Section B: Applied Earth Science, v. 85, p. 170–189.

——2010, Porphyry copper systems: Economic Geology, v. 105, p. 3–41.

Steven, T.A., and Ratte, J.C., 1960, Geology and ore deposits of the Summitville district San Juan Mountains, Colorado: U.S. Geological Survey Professional Paper 343, p. 70.

Suzuki, K., Shimizu, H., and Masuda, A., 1996, Re-Os dating of molybdenites from ore deposits in Japan: Implication for the closure temperature of the Re-Os system for molybdenite and the cooling history of molybdenum ore deposits: Geochimica et Cosmochimica Acta, v. 60, p. 3151–3159.

Swayze, G.A., Clark, R.N., Goetz, A.F.H., Livo, K.E., Breit, G.N., Kruse, F.A., Sutley, S.J., Snee, L.W., Lowers, H.A., Post, J.L., Stoffregen, R.E., and Ashley, R.P., 2014, Mapping advanced argillic alteration at Cuprite, Nevada, using imaging spectroscopy: Economic Geology, v. 109, p. 1179–1221.

Thompson, T.B., 1996, Fluid evolution of the Cripple Creek hydrothermal system, Colorado: Society of Economic Geologists Guidebook Series, v. 26, p. 45–54.

Ueda, A., and Sakai, H., 1984, Sulfur isotope study of Quaternary volcanic rocks from the Japanese islands arc: Geochimica et Cosmochimica Acta, v. 48, p. 1837–1848.

Valencia-Moreno, M., Ochoa-Landín, L., Noguez-Alcántara, B., Ruiz, J., and Pérez-Segura, E., 2007, Geological and metallogenetic characteristics of the porphyry copper deposits of Mexico and their situation in the world context: Geological Society of America Special Papers, v. 422, p. 433–458.

Verati, C., and Jourdan, F., 2014, Effect of sericitization of plagioclase on the $^{40}K/^{40}Ar$ and $^{40}Ar/^{39}Ar$ chronometers: Implication for dating basaltic rocks and mineral deposits, *in* Jourdan, F., Mark, D., and Verati, C., eds., Advances in $^{40}Ar/^{39}Ar$ dating: From archaeology to planetary sciences: Geological Society, London, Special Publication, v. 378, p. 155–174.

Wilson, A.J., Cooke, D.R., and Harper, B.L., 2003, The Ridgeway gold-copper deposit: A high-grade alkalic porphyry deposit in the Lachlan fold belt, New South Wales, Australia: Economic Geology, v. 98, p. 1637–1666.

Wilson, J.W., Cooke, D.R., Benjamin, J.H., and Deyell, C.L., 2007, Sulfur isotopic zonation in the Cadia district, southeastern Australia: Exploration significance and implications for the genesis of alkalic porphyry gold–copper deposits: Mineralium Deposita, v. 42, p. 465–487.

Wolfe, R.C., and Cooke, D.R., 2011, Geology of the Didipio region and genesis of the Dinkidi alkalic porphyry Cu-Au deposit and related pegmatites, Northern Luzon, Philippines: Economic Geology, v. 106, p. 1279–1315.

Woodhead, J.D., Harmon, R.S., and Fraser, D.G., 1987, O, S, Sr, and Pb isotope variations in volcanic rocks from the Northern Mariana Islands: Implications for crustal recycling in intra-oceanic arcs: Earth and Planetary Science Letters, v. 83, p. 39–52.

Yanagisawa, F., and Sakai, H., 1983, Thermal decomposition of barium sulfate-vanadium pentoxide-silica glass mixtures for preparation of sulfur dioxide in sulfur isotope ratio measurements: Analytical Chemistry, v. 55, p. 985–987.

Yang, K., Huntington, J.F., Gemmell, J.B., and Scott, K.M., 2011, Variations in composition and abundance of white mica in the hydrothermal alteration system at Hellyer, Tasmania, as revealed by infrared reflectance spectroscopy: Journal of Geochemical Exploration, v. 108, p. 143–156.

Zukowski, W., 2010, Geology and mineralisation of the Endeavour 41 gold deposit, Cowal District, NSW, Australia: Unpublished PhD thesis, Australia, University of Tasmania, 287 p.

APPENDIX 1

$^{40}Ar/^{39}Ar$ Data

No. step	Temp. (°C)		^{36}Ar	^{37}Ar	^{38}Ar	^{39}Ar	^{40}Ar	Age (ka)	± 2σ	$^{40}Ar(r)$ (%)	$^{39}Ar(k)$ (%)	K/Ca	± 2σ
J value = 0.0007930													
1	500		0.0002219	0.0012308	0.0018488	0.1330298	0.1261554	643.9	± 35.9	47.52	3.84	46.5	± 72.5
2	550	X	0.0003331	0.0045020	0.0048392	0.3441504	0.2654583	690.1	± 21.4	62.61	9.94	32.9	± 14.2
3	600	X	0.0004985	0.0087118	0.0070818	0.5075501	0.3934284	689.9	± 19.7	62.29	14.66	25.1	± 6.0
4	650	X	0.0006154	0.0090005	0.0043652	0.3028677	0.3278312	682.7	± 37.8	44.14	8.75	14.5	± 3.4
5	700	X	0.0004937	0.0096670	0.0024327	0.1689156	0.2225968	642.3	± 80.3	34.11	4.88	7.5	± 1.8
6	750	X	0.0002740	0.0105190	0.0014722	0.1014761	0.1298331	688.0	± 75.9	37.63	2.93	4.1	± 0.8
7	800	X	0.0001450	0.0110733	0.0007701	0.0532191	0.0660594	636.0	± 99.0	35.86	1.54	2.1	± 0.5
8	850	X	0.0001808	0.0121740	0.0008497	0.0592183	0.0820682	702.0	± 127.6	35.45	1.71	2.1	± 0.4
9	900	X	0.0002950	0.0121279	0.0010762	0.0721860	0.1216544	684.3	± 166.9	28.42	2.08	2.6	± 0.4
10	950	X	0.0004177	0.0102383	0.0033287	0.2331545	0.2306860	654.0	± 38.3	46.26	6.73	9.8	± 2.1
11	1,000	X	0.0007683	0.0090024	0.0079000	0.5533540	0.5004941	701.3	± 26.1	54.27	15.98	26.4	± 6.6
12	1,050	X	0.0025263	0.0085536	0.0122465	0.8263897	1.1667334	713.7	± 40.2	35.38	23.86	41.5	± 9.4
13	1,100	X	0.0007105	0.0069414	0.0015739	0.0990933	0.2702370	845.4	± 193.4	21.70	2.86	6.1	± 1.5
14	1,150	X	0.0001341	0.0062779	0.0001386	0.0078932	0.0437493	767.4	± 1935.1	9.69	0.23	0.5	± 0.1
15	1,200	X	0.0000804	0.0060585	0.0000317	0.0007422	0.0220869	2735.5	± 22186.8	6.39	0.02	0.1	± 0.0
		Σ	0.0076944	0.1260783	0.0499552	3.4632400	3.9690721						

Notes: Plateau ages given at the 2σ level are calculated using the mean of all the plateau steps, each weighted by the inverse variance of their individual analytical error; X = steps used for age calculations

APPENDIX 2

Summary of Data for Re-Os Dating of Molybdenite

Description	Sample no.	Re (ppm)	± 2σ	^{187}Re (ppb)	± 2σ	^{187}Os (ppb)	± 2σ	Model age (Ma)	± 2σ with λ (Ma)
Molybdenite	IXCM08-51 210.0	691.6	1.8	434,715	1125	5.651	0.072	0.780	0.010

Notes: The age was constrained using the method described in detail by Selby and Creaser (2004) and Markey et al. (2007); isotopic analysis used a Thermo-Scientific Triton mass spectrometer by Faraday collector at the University of Alberta; Chinese molybdenite powder HLP-5 (Markey et al., 1998), which is used as an in-house control sample by AIRIE, Colorado State University, is also routinely analyzed at the University of Alberta; for this control sample over the period of analysis of the sample, we determined an average Re-Os date of 221.5 ± 0.3 Ma (1σ uncertainty, n = 4); Re-Os age date of 221.0 ± 1.0 Ma is identical to that reported by Markey et al. (1998); molybdenite age was calculated using a ^{187}Re decay constant of 1.666 × 10^{-11} $year^{-1}$ (Smoliar et al., 1996)